

# Multi-site transfer function approach for real-time modeling of the ground electric field induced by laterally-nonuniform ionospheric source

Mikhail Kruglyakov<sup>1</sup>, Elena Marshalko<sup>2</sup>, Alexey Kuvshinov<sup>3</sup>, Maxim Yu Smirnov<sup>4</sup>, and Ari Viljanen<sup>2</sup>

<sup>1</sup>University of Otago

<sup>2</sup>Finnish Meteorological Institute

<sup>3</sup>Institute of Geophysics

<sup>4</sup>Luleå University of Technology

July 8, 2023

## Abstract

We propose a novel approach to model the ground electric field (GEF) induced by laterally-nonuniform ionospheric sources in the real-time. The approach exploits the multi-site transfer function concept, continuous magnetic field measurements at multiple sites in the region of interest, and spatial modes describing the ionospheric source. We compared the modeled GEFs with those measured at two locations in Fennoscandia and observed good agreement between modeled and measured GEF. Besides, we compared GEF-based geomagnetically induced current (GIC) with that measured at the M\“ants\”al\” a natural gas pipeline recording point and again observed remarkable agreement between modeled and measured GIC.

1 **Multi-site transfer function approach for real-time**  
2 **modeling of the ground electric field induced by**  
3 **laterally-nonuniform ionospheric source**

4 **Mikhail Kruglyakov<sup>1,2</sup>, Elena Marshalko<sup>3</sup>, Alexey Kuvshinov<sup>2</sup>, Maxim**  
5 **Smirnov<sup>4</sup>, and Ari Viljanen<sup>3</sup>**

6 <sup>1</sup>University of Otago, Dunedin, New Zealand

7 <sup>2</sup>Institute of Geophysics, ETH Zürich, Zürich, Switzerland

8 <sup>3</sup>Finnish Meteorological Institute, Helsinki, Finland

9 <sup>4</sup>Lulea University of Technology, Lulea, Sweden

10 **Key Points:**

- 11 • Multi-site transfer function approach is proposed for real-time modeling of the ground  
12 electric field induced by laterally-nonuniform source  
13 • The approach exploits magnetic field data from multiple locations and spatial modes  
14 describing the ionospheric source  
15 • Good agreement between modeled and observed GEF and GIC is demonstrated

---

Corresponding author: Mikhail Kruglyakov, [mikhail.kruglyakov@otago.ac.nz](mailto:mikhail.kruglyakov@otago.ac.nz)

## Abstract

We propose a novel approach to model the ground electric field (GEF) induced by laterally-nonuniform ionospheric sources in the real-time. The approach exploits the multi-site transfer function concept, continuous magnetic field measurements at multiple sites in the region of interest, and spatial modes describing the ionospheric source. We compared the modeled GEFs with those measured at two locations in Fennoscandia and observed good agreement between modeled and measured GEF. Besides, we compared GEF-based geomagnetically induced current (GIC) with that measured at the Mäntsälä natural gas pipeline recording point and again observed remarkable agreement between modeled and measured GIC.

## Plain Language Summary

The Earth’s magnetic field disturbances, like geomagnetic storms and magnetospheric substorms, generate geomagnetically induced currents (GIC) in technological systems like power grids. GIC calculation is of practical interest since, in some cases, GIC can cause power grid blackouts. An accurate GIC calculation, preferably in real-time, requires knowledge of the ground electric field (GEF) along power lines. The GEF is rarely measured directly, so it needs to be simulated using, as realistic as possible, models of the Earth’s electrical conductivity and the source responsible for geomagnetic disturbances. This study presents and validates a novel approach to model the GEF in real-time, which exploits – in a non-conventional way – magnetic field measurements at multiple sites in the region of interest.

## 1 Introduction

According to Faraday’s law, the large fluctuations of the Earth’s magnetic field during geomagnetic storms and magnetospheric substorms generate the ground electric field (GEF), which in turn drives the so-called geomagnetically induced currents (GIC) in ground-based technological systems, such as power grids and pipelines (Viljanen & Pirjola, 1994). GIC calculation is of practical interest since, in the worst case, GIC can cause the transformers’ destructions lead to power grid blackouts, as it happened, for example, in the Malmö region in Sweden on 30 October 2003 (Pulkkinen et al., 2005) and in Otago region in New Zealand on 6 November 2001 (Marshall et al., 2012; Rodger et al., 2017). An accurate calculation of GIC variations, ideally in real-time, requires knowledge of the spatio-temporal evolution of ground electric field (GEF) along power/pipelines. However, GEF measurements are occasional and, if they exist, usually last a few months at most. So the only alternative is the numerical simulation of the GEF.

The majority of the studies in connection with GEF or GIC simulations are based on the simplest model of the source, i.e. the laterally uniform one, and, often, but not always, on the laterally uniform conductivity distribution model (e.g. Wang et al. (2016); Divett et al. (2017); Kelbert et al. (2017); Bailey et al. (2018); Nakamura et al. (2018); Marshall et al. (2019); Rosenqvist and Hall (2019); Divett et al. (2020)). The intermediate approach for the use of a non-uniform source without the full simulations for one is used in (Viljanen et al., 2012), (Campanyà et al., 2019) and (Malone-Leigh et al., 2023), where the relations between electric and magnetic fields are based on plane-wave assumption, while the magnetic field is obtained by the interpolation from few observation sites. As for the full simulations with non-uniform sources, there are just a few of them (e.g. Beggan (2015); Honkonen et al. (2018); Marshalko et al. (2020, 2021); Beggan et al. (2021)).

Very recently Kruglyakov, Kuvshinov, and Marshalko (2022) proposed a method for real-time modeling of the GEF induced by laterally-varying ionospheric sources. Their technique is based on the isolation of the inducing source (approximated by ionospheric sheet current) using the Spherical Elementary Current System (SECS) approach (Vanhamäki

65 & Juusola, 2020) as applied to the magnetic field variations simultaneously recorded at  
 66 a regional network of observations. Further, the source is factorized by spatial modes (SM)  
 67 and respective time-varying expansion coefficients using time-domain Principal Compo-  
 68 nent Analysis (PCA) of SECS-recovered inducing current.

69 The SECS approach can be viewed as a regional variant of the Gauss method —  
 70 the method used to separate the inducing and induced signals on a global scale. If the  
 71 region of interest is characterized by 3-D conductivity distribution, the induced part is  
 72 inevitably influenced by 3-D effects arising, particularly from the lateral (for example,  
 73 land/ocean) conductivity contrasts. Given the usually deficient spatial distribution of  
 74 the magnetic field observations, the SECS approach precludes an accurate description  
 75 of the induced part affected by localized 3-D effects. Such imperfection in the induced  
 76 part description also influences the recovery of the inducing part in terms of the recovery  
 77 of the time series of expansion coefficients.

78 To circumvent this problem Marshalko et al. (2023) introduced an approach to es-  
 79 timate expansion coefficients more accurately. The approach also exploits the spatial modes  
 80 resulting from the PCA of SECS-recovered inducing source, but an estimation of the ex-  
 81 pansion coefficients is performed using a 3-D conductivity model of the region. However,  
 82 the disadvantage of their method is a high computational load to obtain expansion co-  
 83 efficients, thus precluding its implementation for real-time GEF modeling.

84 This paper proposes a method that also works with spatial modes but avoids es-  
 85 timating the expansion coefficients. An approach is based on the multi-site (MS) trans-  
 86 fer function (TF) concept where MS TF relate the GEF at any location with a horizon-  
 87 tal components of magnetic field at (fixed) multiple locations. Notably, an approach al-  
 88 lows researchers to model the GEF in real time. The proposed technique can be consid-  
 89 ered a generalization of the inter-site TF formalism presented in (Kruglyakov, Kuvshi-  
 90 nov, & Nair, 2022). In their paper, TFs relate sea-bed and single-site land-based mag-  
 91 netic fields, and spatial modes are obtained from spherical harmonic analysis of the mag-  
 92 netic data recorded at a global network of geomagnetic observatories.

93 Using Fennoscandia as a study region, we validate the MS TF approach by compar-  
 94 ing modeled and measured GEF and GIC time series. The reasons for selecting this  
 95 high-latitude region are manifold. First, technological systems in polar regions are es-  
 96 pecially vulnerable due to the excessive GIC. Second, the inducing source at high lat-  
 97 itudes reveals significant lateral variability, which we are interested in accounting for in  
 98 our approach. Third, the 3-D electrical conductivity model is available for Fennoscan-  
 99 dia (Korja et al., 2002). Fourth, there is a magnetometer network in the region (Inter-  
 100 national Monitor for Auroral Geomagnetic Effect, IMAGE (Tanskanen, 2009)), which  
 101 provides long-term, simultaneous and continuous measurements of the magnetic field at  
 102 multiple locations — the prerequisite data for successfully applying the proposed approach.  
 103 Moreover, in Fennoscandia, one can find relatively long (from weeks to months) contin-  
 104 uous GEF measurements performed during magnetotelluric surveys in the region. Fi-  
 105 nally, GIC observations have been carried out at the Mäntsälä natural gas pipeline record-  
 106 ing point starting from November 1998 (Viljanen et al., 2006), allowing us to compare  
 107 observed and modeled GIC for several space weather events.

## 108 2 Methodology

We assume that the horizontal ground electric field  $\mathbf{E}_h = (E_x, E_y)$  at any loca-  
 tion is related in the frequency domain to  $\mathbf{B}_h = (B_x, B_y)$  at  $N$  sites as

$$\mathbf{E}_h(\mathbf{r}, \omega; \sigma) = \sum_{k=1}^N \Lambda(\mathbf{r}, \mathbf{r}_k, \omega; \sigma) \mathbf{B}_h(\mathbf{r}_k, \omega; \sigma), \quad (1)$$

109 where  $x$  and  $y$  are directed to geographic North and East, respectively.

A set of  $\Lambda_k \equiv \Lambda(\mathbf{r}, \mathbf{r}_k, \omega; \sigma)$  is called multi-site transfer function, where each  $\Lambda_k$  is the following  $2 \times 2$  matrix

$$\Lambda_k = \begin{pmatrix} \Lambda_{xx,k} & \Lambda_{xy,k} \\ \Lambda_{yx,k} & \Lambda_{yy,k} \end{pmatrix}. \quad (2)$$

Estimating the elements of matrices  $\Lambda_k$ ,  $k = 1, 2, \dots, N$  at a given frequency  $\omega$  and conductivity model  $\sigma$  is performed as follows. First, one calculates the fields  $\mathbf{B}^{(l)}(\mathbf{r}_k, \omega; \sigma)$  and  $\mathbf{E}^{(l)}(\mathbf{r}, \omega; \sigma)$  corresponding to  $l$ -th spatial modes  $\mathbf{j}_l(\mathbf{r})$  describing the inducing (extraneous) source

$$\mathbf{j}^{\text{ext}}(\mathbf{r}, t) = \sum_{l=1}^L c_l(t) \mathbf{j}_l(\mathbf{r}), \quad (3)$$

where  $L$  stands for a number of spatial modes. Then the elements of  $\Lambda_k$  are estimated row-wise using the calculated  $\mathbf{B}_h^{(l)}$  and  $\mathbf{E}_h^{(l)}$  fields. Specifically, elements of  $\Lambda_k$  are obtained as the solution of the following two systems of linear equations (SLE)

$$\Lambda_{xx,1} B_x^{(l)}(\mathbf{r}_1) + \Lambda_{xy,1} B_y^{(l)}(\mathbf{r}_1) + \dots + \Lambda_{xx,N} B_x^{(l)}(\mathbf{r}_N) + \Lambda_{xy,N} B_y^{(l)}(\mathbf{r}_N) = E_x^{(l)}(\mathbf{r}), \quad (4)$$

and

$$\Lambda_{yx,1} B_x^{(l)}(\mathbf{r}_1) + \Lambda_{yy,1} B_y^{(l)}(\mathbf{r}_1) + \dots + \Lambda_{yx,N} B_x^{(l)}(\mathbf{r}_N) + \Lambda_{yy,N} B_y^{(l)}(\mathbf{r}_N) = E_y^{(l)}(\mathbf{r}), \quad (5)$$

110 where  $l = 1, 2, \dots, L$ . Note, that in Equations (4) and (5) the dependency of all quan-  
 111 tities on  $\omega$ ,  $\mathbf{B}_h^{(l)}$  and  $\mathbf{E}_h^{(l)}$  on  $\sigma$ , and elements of  $\Lambda_k$  on  $\sigma$ ,  $\mathbf{r}$  and  $\mathbf{r}_k$  are omitted but im-  
 112 plied. To resolve the TF, the number of spatial modes,  $L$ , should be equal to or larger  
 113 than the doubled number of the sites,  $N$ , i.e.  $L \geq 2N$ . Also, our model experiments  
 114 indicate that the condition number of the system matrices in Equations (4) and (5) can  
 115 be quite large, so we used the regularized ordinary least squares approach to solve the  
 116 above SLEs.

Once elements of  $\Lambda_k$  are estimated at a predefined number of frequencies, the GEF at a given time instant  $t_i = i\Delta t$  and a given location  $\mathbf{r}$  is then calculated using a numerical scheme similar to that described by Marshalko et al. (2023)(cf. Equation 20 of that paper), namely

$$\mathbf{E}_h(\mathbf{r}, t_i; \sigma) = \sum_{n=0}^{N_t} \sum_{k=1}^N \Lambda^{(n)}(\mathbf{r}, \mathbf{r}_k, T_\Lambda; \sigma) \mathbf{B}_h^{\text{obs}}(\mathbf{r}_k, t_i - n\Delta t), \quad (6)$$

where  $\mathbf{B}_h^{\text{obs}}$  stands for horizontal components of the observed field in corresponding locations and  $N_t = T_\Lambda / \Delta t$ . As discussed in (Marshalko et al., 2023), computation of quantities like  $\Lambda^{(n)}(\mathbf{r}, \mathbf{r}_k, T_\Lambda; \sigma)$  can be reduced to the estimation of the following integrals

$$\Lambda^{(n)}(\mathbf{r}, \mathbf{r}_k, T_\Lambda; \sigma) = \text{Re} \left\{ \frac{\Delta t}{\pi} \int_0^{\frac{\pi}{\Delta t}} \Lambda(\mathbf{r}, \mathbf{r}_k, \omega; \sigma) e^{-i\omega n \Delta t} d\omega \right\}, \quad n = 1, 2, \dots, N_\Lambda - 1. \quad (7)$$

117 Expressions for  $\Lambda^{(0)}$  and  $\Lambda^{N_\Lambda}$  are more complicated, but their calculation is similar to  
 118 that presented in Appendix A of (Marshalko et al., 2023) to calculate the correspond-  
 119 ing terms for the electric field.

120 Computation of the integrals in Equation (7) is performed as follows. First,  $\Lambda(\mathbf{r}, \mathbf{r}_k, \omega; \sigma)$   
 121 are computed at  $N_f$  logarithmically spaced frequencies from  $f_{\min}$  to  $f_{\max}$  using Equations (4) and (5).  
 122 Further, one can analytically compute the corresponding integrals by exploiting cubic spline interpolation  
 123 as applied to calculated  $\Lambda$ . Our model experiments  
 124 (not shown in the paper) indicate that  $N_f = 71$ ,  $f_{\min} = 6.13 \cdot 10^{-7}$  Hz, and  $f_{\max} = 0.054$  Hz  
 125 provide an accurate estimation of the integrals, in the assumption that  $\Delta t$  is taken as 10 s.

126 As seen from Equations (4) and (5), the estimation of  $\Lambda(\mathbf{r}, \mathbf{r}_k, \omega; \sigma)$  requires spec-  
 127 ification of  $\mathbf{j}_l, l = 1, 2, \dots, L$ . The form of  $\mathbf{j}_l$  (and their number,  $L$ ) varies with the ap-  
 128 plication. As discussed in Introduction, in this paper, we use spatial modes obtained by  
 129 means of the time-domain Principal Component Analysis (PCA) of the SECS-recovered  
 130 inducing source. The reader can find further details on the derivation of these modes in  
 131 the next section.

132 As also seen from Equations (4) and (5) (and already mentioned before), the es-  
 133 timation of  $\Lambda(\mathbf{r}, \mathbf{r}_k, \omega; \sigma)$  implies computations of  $\mathbf{B}^{(l)}(\mathbf{r}_k, \omega; \sigma)$  and  $\mathbf{E}^{(l)}(\mathbf{r}, \omega; \sigma)$  in a given  
 134 conductivity model  $\sigma$  of the region of interest. We performed these computations using  
 135 the scalable 3-D EM forward modeling code PGIEM2G (Kruglyakov & Kuvshinov, 2018)  
 136 based on a method of volume integral equation.

137 Worth noting that quantities  $\Lambda^{(n)}(\mathbf{r}, \mathbf{r}_k, T_\Lambda; \sigma), n = 0, 1, \dots, N_t$  are time-invariant,  
 138 and for a given conductivity model are calculated only once, then stored and used when  
 139 the calculation of  $\mathbf{E}_h(\mathbf{r}, t; \sigma)$  is required.

140 It is also important to note that the “memory”  $T_\Lambda$  can be taken as short as 15 min  
 141 (at least for Fennoscandia – the region we have selected to validate the presented approach).  
 142 Namely, a small value for  $T_\Lambda$  allows us to calculate  $\mathbf{E}_h(\mathbf{r}, t; \sigma)$  in real time, provided long-  
 143 term continuous observations of the magnetic field,  $\mathbf{B}_h^{\text{obs}}$  are available at multiple loca-  
 144 tions. Further justification of  $T_\Lambda$  smallness is presented in the following two sections.

145 Ideally,  $\Lambda$  should relate the electric field with the magnetic field measured at as large  
 146 as possible number of sites. However, there are usually gaps in the magnetic field data.  
 147 At the same time, to apply the presented methodology, one needs to use continuous time  
 148 series of magnetic field during the interval  $[t_i - T_\Lambda, t_i]$  to compute  $\mathbf{E}_h(\mathbf{r}, t_i; \sigma)$ . Thus one  
 149 has to choose observatories accordingly to continuous data availability. However, one can  
 150 use different (precomputed) sets of  $\Lambda$  for different time instances  $t_i$ . Combining this op-  
 151 tion with the short  $T_\Lambda$  means that the number of sites with magnetic field observations  
 152 in use is always large enough to implement the proposed approach.

153 The final remark of this section is that if the spatial modes are just two polariza-  
 154 tions of vertically indenting plane wave, then  $\Lambda$  degenerates to intersite impedance  $Z$ ;  
 155 cf. Section 2.2 of (Marshalko et al., 2023).

## 156 3 Results

### 157 3.1 3-D conductivity model

158 One of the critical components required for as realistic as feasible GEF modeling  
 159 is a trustworthy conductivity model of the Earth’s subsurface in the region of interest.  
 160 The conductivity model of Fennoscandia we adopt comprises a 3-D part (upper 60 km  
 161 below the surface of the Earth) and the 1-D part underneath taken as a corresponding  
 162 piece (deeper than 60 km) of the 1-D profile from (Kuvshinov et al., 2021). As for the  
 163 3-D part, it is based on the SMAP model (Korja et al., 2002), covers the area of  $2550 \times$   
 164  $2550 \text{ km}^2$  and consists of three layers of laterally variable conductivity of 10, 20, and 30  
 165 km thicknesses. The lateral discretization of the model is  $512 \times 512$  cells, meaning that  
 166 cells’ size is about  $5 \times 5 \text{ km}^2$ . Note that this model (of the same discretization) was also  
 167 used in (Marshalko et al., 2021; Kruglyakov, Kuvshinov, & Marshalko, 2022; Marshalko  
 168 et al., 2023). The interested reader can find details on the conductivity distribution in  
 169 the model, for example, in (Kruglyakov, Kuvshinov, & Marshalko, 2022), cf. their Fig-  
 170 ure 7. Note also that for  $T_\Lambda$  calculations only observatories located in the area covered  
 171 by this model are used, i.e. not all IMAGE observatories.

172

### 3.2 Deriving spatial modes

173

174

175

As mentioned in the Introduction, spatial modes  $\mathbf{j}_l(\mathbf{r})$  are obtained using the SECS method and their derivation involves the following two steps (Kruglyakov, Kuvshinov, & Marshalko, 2022):

176

177

178

179

180

181

182

183

1. Spherical Elementary Current Systems (SECS) method (Vanhamäki & Juusola, 2020) is applied to 29–31 October 2003 (Halloween storm) ten-second IMAGE magnetic field data to separate the inducing and induced current systems that are assumed to flow 90 km above the Earth’s surface and 1 m below the Earth’s surface, correspondingly. The data from all 26 magnetometers were used to perform the SECS analysis. The locations of IMAGE magnetometers in use are demonstrated in Figure 1. Note that IMAGE data for this 72-hour time interval contain several gaps; linear interpolation was applied to fill these gaps.

184

185

186

2. The time-domain PCA is applied to the SECS-recovered inducing source resulting in the desired  $\mathbf{j}_l(\mathbf{r}), l = 1, 2, \dots, L$ . With  $L = 34$ , we described 99.9% of the inducing source variability.

187

188

189

190

191

192

193

194

195

It is relevant to mention that later in the paper, we analyze the data from the Halloween storm and other space weather events. One can argue that  $\mathbf{j}_l$  obtained for a specific event could be non-adequate for other events. Kruglyakov, Kuvshinov, and Marshalko (2022) addressed this question and demonstrated that irrespective of the event (which corresponds to sources of different geometry), the spatial structure of these sources is well approximated by a finite number of  $\mathbf{j}_l$  obtained from the analysis of some specific event (in our case the Halloween storm). The prerequisite to getting an adequate set of  $\mathbf{j}_l$  is that the event for their estimation should be long enough and sufficiently energetically large and spatially complex.

196

### 3.3 Comparing modeled and observed GEF

197

198

199

200

201

202

203

204

205

206

207

208

209

210

211

212

213

214

215

216

217

218

219

220

Even though there are multiple locations in Fennoscandia where continuous ground electric field measurements were performed for relatively long time intervals (from weeks to months), our analysis of the available data reveals that most of the GEF observations were conducted during periods of relatively quiet geomagnetic activity. Note that the potentially hazardous GIC are flowing in the technological systems during geomagnetic disturbances like geomagnetic storms and magnetospheric substorms, making such space weather events of particular interest in the context of this study. Fortunately, continuous (one-second) GEF measurements performed in August 2005 – June 2006 at 8 of 13 sites around Joensuu, Finland, in the framework of Electromagnetic Mini Array (EMMA) Project (Smirnov et al., 2006) have successfully recorded prominent space weather event – magnetospheric substorm of 11 September 2005; during this event, amplitudes of the observed GEF in the region exceeded 2000 mV/km. We compare modeled and measured time series of the GEF during this event at two sites (denoted below as M02 and M05) where the largest GEF amplitudes were observed and where the data quality – in terms of absence of gaps, jumps, and electrodes’ drift – was the highest. The comparison is performed for the time interval from 05:15 UT to 6:15 UT. This interval includes a 30-min long event and 15-min long quiet periods before and after the event. During this time interval, 16 IMAGE observation sites delivered uninterrupted magnetic field recordings, and thus, only the data from these sites were used to calculate the GEF using Equation (6). Figure 2 shows the location of these IMAGE sites (blue circles) and two sites (red circles) with GEF recordings selected for comparison of the observed and modeled GEF. Since GEF measurements were performed in geomagnetic coordinates, we decided to compare observed and modeled GEF components in this coordinate system. Thus, in this section, the  $x$ - and  $y$ -components of the GEF are geomagnetic North and East compo-

221 nents, respectively. Besides, experimental 1-sec time series of the GEF were re-sampled  
 222 to a 10-sec time series to make them compatible with IMAGE magnetic field data.

It is important to note here that depending on location, the modeled GEF might still over- or underestimate the amplitudes of the actual GEF. This is due to galvanic effects, i.e. the build-up of electric charges along local near-surface heterogeneities (Jiracek, 1990) that cannot be included in the model. Galvanic effects are commonly accounted for with a  $2 \times 2$  real-valued time-independent – unique for each location – distortion matrix,  $D$ , which linearly relates observed  $\mathbf{E}_h^{\text{obs}}$  and modeled  $\mathbf{E}_h^{\text{mod}}$  electric fields as (Pütke et al., 2014)

$$\mathbf{E}_h^{\text{obs}}(\mathbf{r}, t) = D(\mathbf{r})\mathbf{E}_h^{\text{mod}}(\mathbf{r}, t), \quad D(\mathbf{r}) = \begin{pmatrix} D_{xx} & D_{xy} \\ D_{yx} & D_{yy} \end{pmatrix}. \quad (8)$$

Having observed and calculated GEF at many time instants and bearing in mind that  $D$  is time-independent, we can form highly over-determined SLE given by Equation (8) to estimate elements of  $D$  using the least-square method. Specifically, these elements are estimated row-wise as the solutions of the following two SLEs

$$D_{xx}E_x^{\text{mod}}(t_i) + D_{xy}E_y^{\text{mod}}(t_i) = E_x^{\text{obs}}(t_i), \quad (9)$$

and

$$D_{yx}E_x^{\text{mod}}(t_i) + D_{yy}E_y^{\text{mod}}(t_i) = E_y^{\text{obs}}(t_i), \quad (10)$$

223 where  $t_i$  runs multiple ( $K$ ) time instants. Note that the dependence of all quantities in  
 224 Equations (9) and (10) on  $\mathbf{r}$  is omitted but implied. To make the comparison as fair as  
 225 possible, we calculated distortion matrices using the data not from the time interval where  
 226 we compare the results (05:15 – 06:15 September 11) but using the data far before the  
 227 event, specifically, namely the data from one (whole; September 9) day, giving  $K = 24 \times$   
 228  $3600/10 = 8640$  equations to estimate respective two elements.

As stated in the previous section, the memory  $T_\Lambda$  can be taken as short as 15 min in Equation (6). To explore whether this is the case, we performed GEF calculations taking  $T_\Lambda$  as 15, 30, 60 and 90 min. Figures 3 and 4 compare observed and (corrected for the distortion) modeled  $E_x$  and  $E_y$ , respectively, at sites M02 and M05 for different values of  $T_\Lambda$ . Note that the corrected modeled GEF are calculated by reusing Equation (8), i.e., as

$$\mathbf{E}_h^{\text{mod,corr}}(\mathbf{r}, t) = D(\mathbf{r})\mathbf{E}_h^{\text{mod}}(\mathbf{r}, t), \quad (11)$$

229 where elements of  $D$  are obtained from the solution of the SLEs (9) and (10). As is seen,  
 230 the modeled results for all values of  $T_\Lambda$  are indistinguishably similar, meaning that  $T_\Lambda$   
 231 can be taken as 15 min. Tables 1 and 2 confirm this inference more quantitatively by  
 232 showing correlation coefficients and coefficients of determination at sites M02 and M05,  
 233 respectively, for the considered 1-hour time interval. One can see that both quantities  
 234 practically do not differ with respect to the value of  $T_\Lambda$ .

235 What is also noticeable from the tables is that the agreement between experimen-  
 236 tal and modeled GEF (in terms of both correlation coefficients and coefficients of deter-  
 237 mination) is better in the  $E_y$  component. This is most probably because the ionospheric  
 238 current (source) flows predominantly in the  $y$  direction, making GEF modeling in this  
 239 direction more accurate. Returning to Figures 3 and 4, we also observe that the exper-  
 240 imental GEF at selected sites separated by only 21 km significantly differ, more consid-  
 241 erably than the modeled GEF. The most probable reason for this is the existence of lo-  
 242 cal 3-D conductivity heterogeneities in this region which are not accounted for in the avail-  
 243 able 3-D conductivity model of the region.

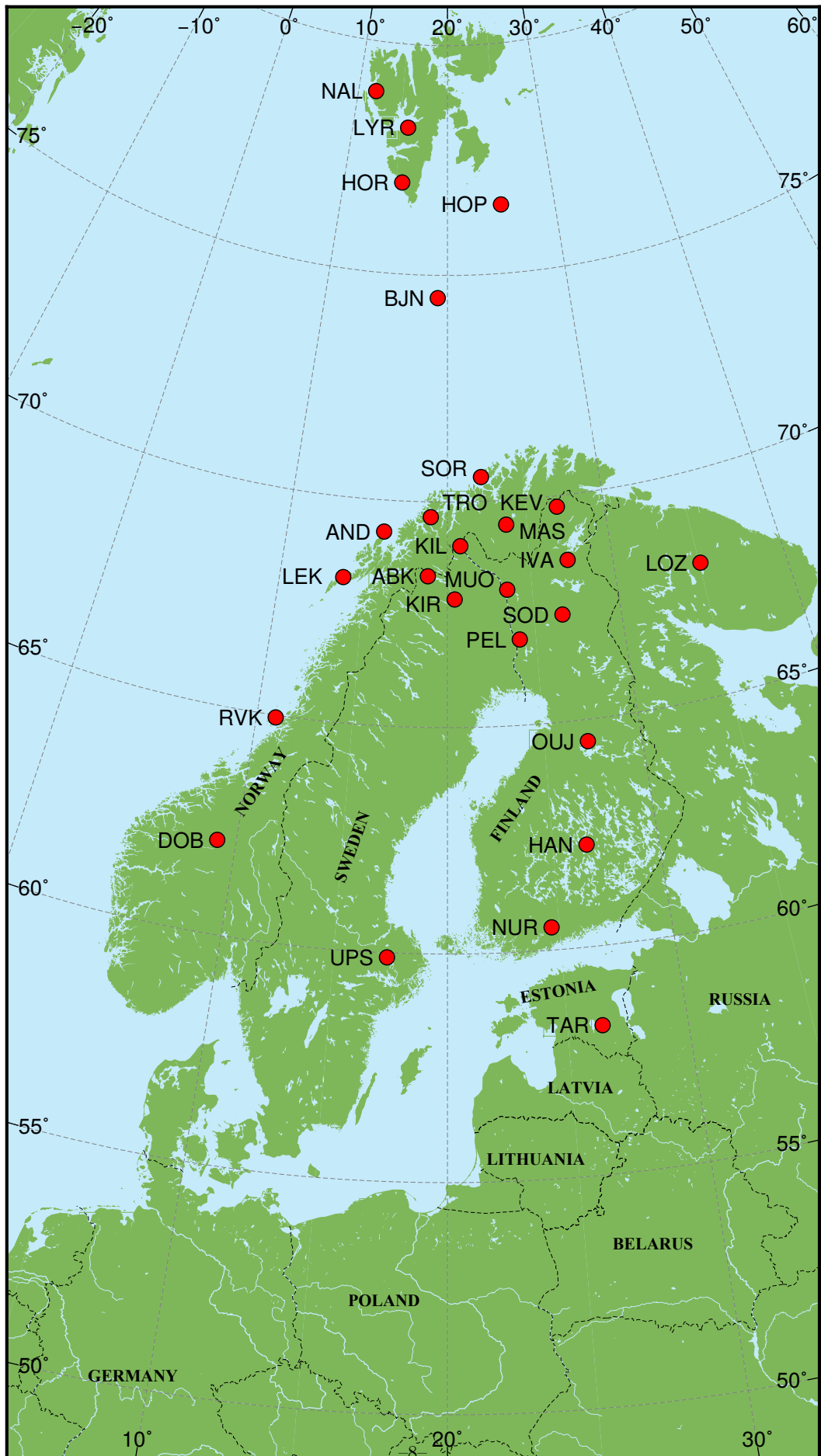


**Figure 1.** Location of IMAGE observatories with available data for 29 – 31 October 2003.

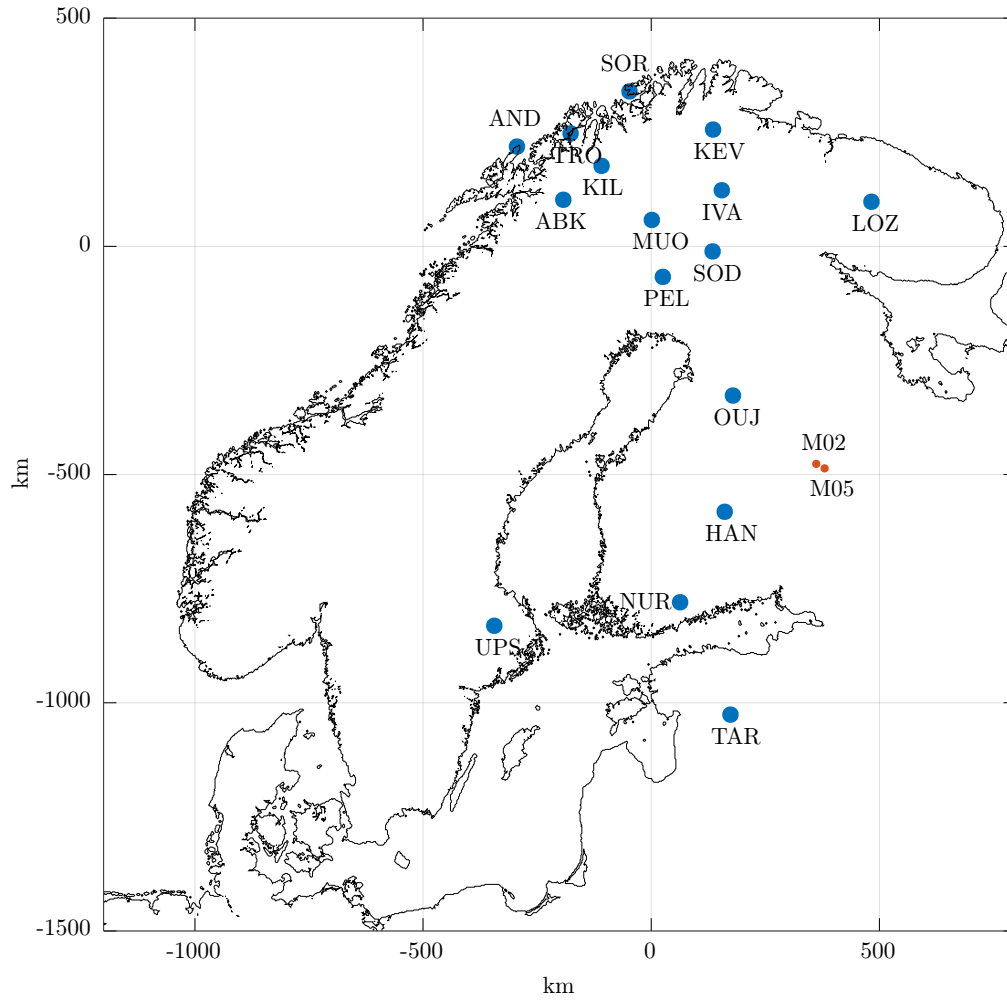


**Figure 2.** Location of IMAGE sites (blue-filled circles) used for GEF simulation (see Equation 6). Red circles – the location of sites where the GEF was measured and used for comparison with the simulated GEF.

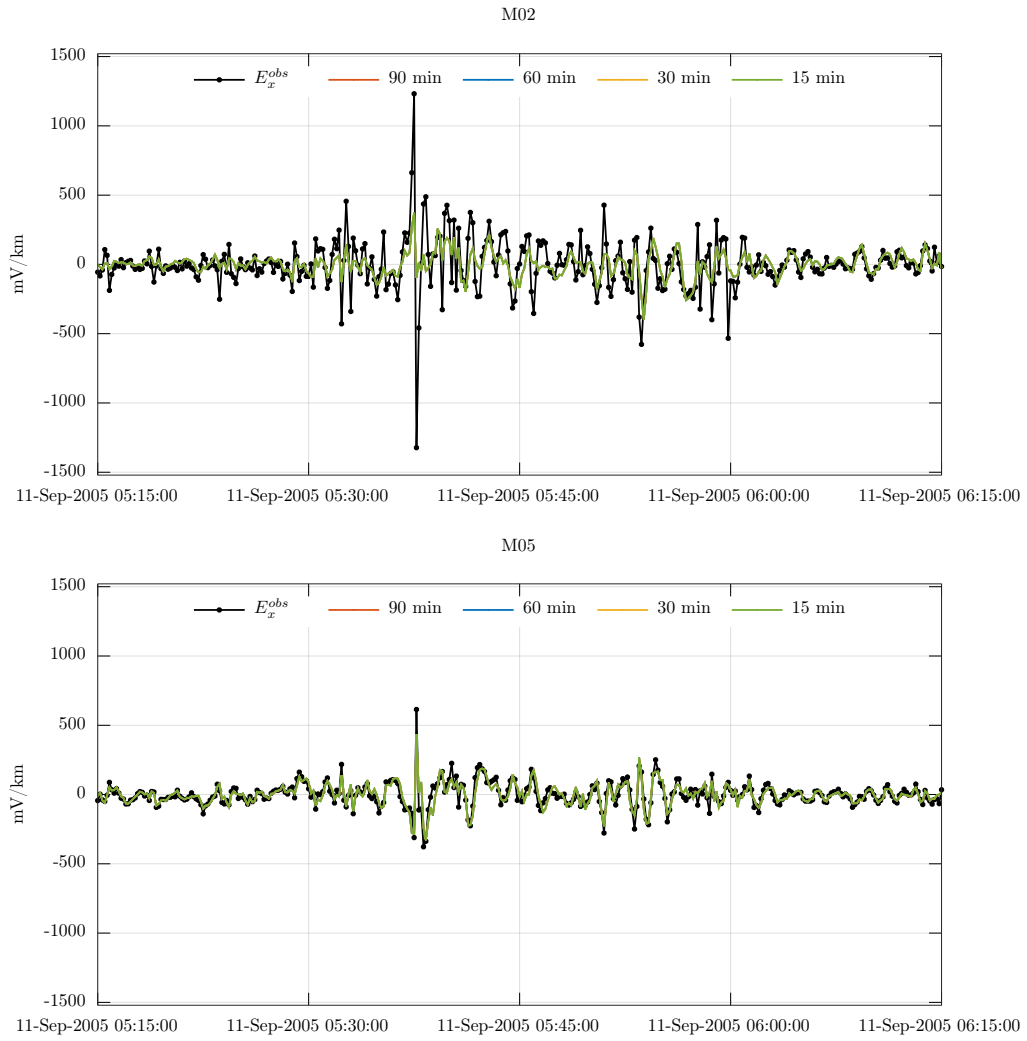


**Figure 3.** Comparison of the (geomagnetic) northward component of observed and modeled GEF at M02 and M05 sites for different values of  $T_{\Lambda}$ .

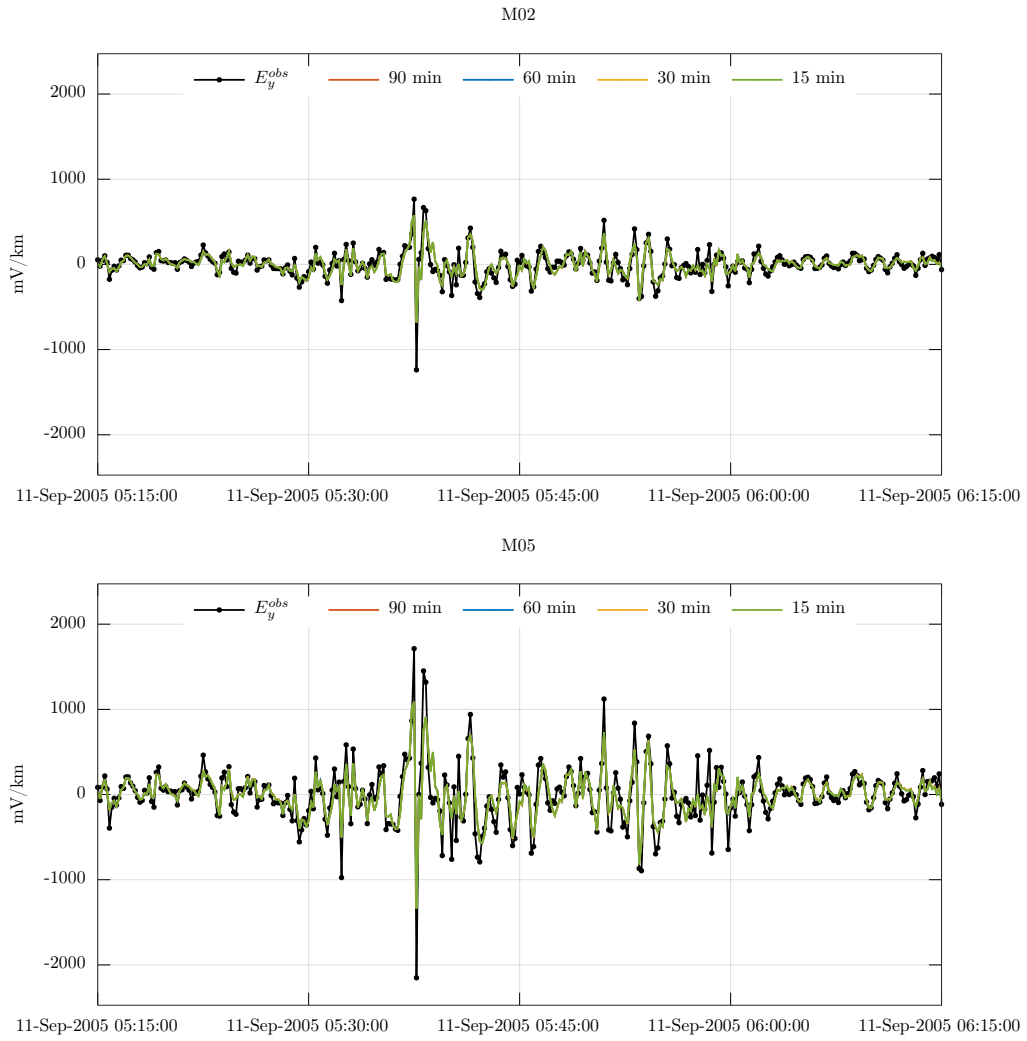


**Figure 4.** Comparison of the (geomagnetic) eastward component of observed and modeled GEF at M02 and M05 sites for different values of  $T_{\Lambda}$ .

**Table 1.** The agreement between modeled and observed GEF at site M02 in terms of correlation coefficients and coefficients of determination.

$T_\Lambda$ , min	Corr for $E_x$	Corr for $E_y$	$R^2$ for $E_x$	$R^2$ for $E_y$
15	0.635	0.881	0.371	0.768
30	0.633	0.881	0.370	0.767
60	0.632	0.881	0.369	0.767
90	0.632	0.880	0.369	0.766

**Table 2.** The agreement between modeled and observed GEF at site M05 in terms of correlation coefficients and coefficients of determination.

$T_\Lambda$ , min	Corr for $E_x$	Corr for $E_y$	$R^2$ for $E_x$	$R^2$ for $E_y$
15	0.882	0.891	0.777	0.767
30	0.882	0.890	0.778	0.766
60	0.882	0.890	0.778	0.766
90	0.882	0.890	0.778	0.766

244

#### 4 Comparing observed and modeled GIC

The conventional approach to simulate GIC in the pipelines is based on the following linear model (Boteler, 2013; Boteler & Pirjola, 2014)

$$GIC(\mathbf{r}, t) = \sum_{i=1}^M [a_i(\mathbf{r})E_x(\mathbf{r}_i, t) + b_i(\mathbf{r})E_y(\mathbf{r}_i, t)], \quad (12)$$

where  $M$  is the number of pipeline nodes and ends,  $\mathbf{r}_i$  – coordinates of their location, and  $\mathbf{r}$  is the coordinate of the pipeline point where GIC is recorded. Note that coefficients  $a_i$  and  $b_i$  are time-independent, but depend on pipeline physical parameters. In case when the conductivity distribution and the source are both laterally uniform, Equation (12) degenerates to

$$GIC(\mathbf{r}, t) = a(\mathbf{r})E_x(\mathbf{r}, t) + b(\mathbf{r})E_y(\mathbf{r}, t). \quad (13)$$

245

246

247

248

The formula (13) has been used in many studies (for example, Pulkkinen et al. (2001); Trichtchenko and Boteler (2002); Wawrzaszek et al. (2023)), but due to the obvious lateral nonuniformity of the conductivity distribution and the source in the region under investigation, we use Equation (12) to calculate GIC.

Having observed GIC and calculated GEF at many time instants, and bearing in mind that coefficients  $a_i$  and  $b_i$  are time-independent, we can form – as for elements of matrix  $D$  discussed in the previous section – highly over-determined SLE given by Equation (12) to estimate coefficients using the least-squares method. Precisely, these coefficients are calculated as the solution of the following SLE

$$a_1 E_x^{\text{mod}}(\mathbf{r}_1, t_i) + b_1 E_y^{\text{mod}}(\mathbf{r}_1, t_i) + \dots + a_M E_x^{\text{mod}}(\mathbf{r}_M, t_i) + b_M E_y^{\text{mod}}(\mathbf{r}_M, t_i) = GIC^{\text{obs}}(t_i), \quad (14)$$

249

250

251

252

253

where  $t_i$  runs multiple ( $K$ ) time instants. Here we omit the dependence of the coefficients and  $GIC^{\text{obs}}$  on  $\mathbf{r}$  because we have GIC's recordings only at one (Mäntsälä; MAN) point. Figure 5 shows the general geometry of the pipeline (gray lines) and location of 18 pipeline's nodes and ends (gold diamonds). The geometry of the pipeline is based on models presented in (Pulkkinen et al., 2001) and (Dimmock et al., 2019).

254

255

GIC measurements at the Mäntsälä point have been performed continuously since 1999; thus, we had an opportunity to compare observed and modeled GIC for a number of events.

**Table 3.** The agreement between modeled and observed GIC in terms of correlation coefficients and coefficients of determination for different events (substorms).

Substorms	Correlation	$R^2$
15 July – 16 July 2000	0.909	0.826
05 November – 06 November 2001	0.895	0.782
29 October – 1 November 2003	0.936	0.871

256 We have chosen events that happened in 2000, 2001, and 2003 years. It should be noted  
 257 that the approach we use to determine coefficients  $a_i$  and  $b_i$  is implicitly based an as-  
 258 sumption that the configuration of the pipeline system was the same during the events  
 259 in study. Concerning the relatively short period of 2000 – 2003, no major modifications  
 260 of the pipeline network were made. However, the present pipeline system is more exten-  
 261 sive than in the beginning of 2000's.

Note also that from 2005 the quality of GIC measurements degraded; this is why we considered earlier years' events. Also, note that the modeled GIC are calculated by reusing Equation (12)

$$GIC^{\text{mod}}(t) = \sum_{i=1}^M [a_i E_x^{\text{mod}}(\mathbf{r}_i, t) + b_i E_y^{\text{mod}}(\mathbf{r}_i, t)], \quad (15)$$

262 where  $a_i$  and  $b_i$  are obtained from the solution of the SLE (14). GEF in Equation (15)  
 263 were calculated using  $T_\Lambda = 15$  min; our model experiments (not shown in the paper) with  
 264 larger  $T_\Lambda$  reveal a negligible difference in the modeled GIC. As in the case of the GEF  
 265 comparison discussed in the previous section, we estimated  $a_i$  and  $b_i$  using GIC data not  
 266 from the time interval where we compare the results but using continuous data for 27 –  
 267 28 October 2003, giving  $K = 2 \times 24 \times 3600/10 = 17280$  equations to estimate respec-  
 268 tive  $2 \times M = 36$  coefficients.

269 Top two panels in Figures 6 – 8 demonstrate time series of observed and modeled  
 270 GIC for two 3-hour time intervals of corresponding years/months when large fluctuations  
 271 of GIC were detected. As one can see, the agreement between observed and modeled GIC  
 272 is remarkably good. The bottom right panels in the figures demonstrate the agreement  
 273 differently. It shows cross-plots of the observed and modeled GIC. Ideally, the observed  
 274 and modeled GIC would lie in a straight line, and this is indeed the case. Note that the  
 275 bottom left panel shows IMAGE observatories, the data from which were used to calcu-  
 276 late the GEF using Equation (6).

277 Finally, Table 3 demonstrates the agreement in a more quantitative way by pre-  
 278 senting correlation coefficients and coefficients of determination for the considered events.  
 279 One can see that both coefficients are close to 1, irrespective of the event. Interestingly,  
 280 the agreement in GIC is better than in GEF (see previous section). We attribute bet-  
 281 ter agreement in GIC to a smoothing effect of summation (see Equation (15)) which ef-  
 282 fectively suppresses the potential inaccuracy of modeled GEF at considered nodes and  
 283 ends.

## 284 5 Conclusions

285 This paper presents a novel approach to the GEF calculation in real time. The ap-  
 286 proach makes it possible to take into account the 3-D Earth's conductivity distribution  
 287 in the region and lateral variability of the source. It works with spatial modes describ-  
 288 ing the spatial structure of the source and exploits the multi-site (MS) transfer function

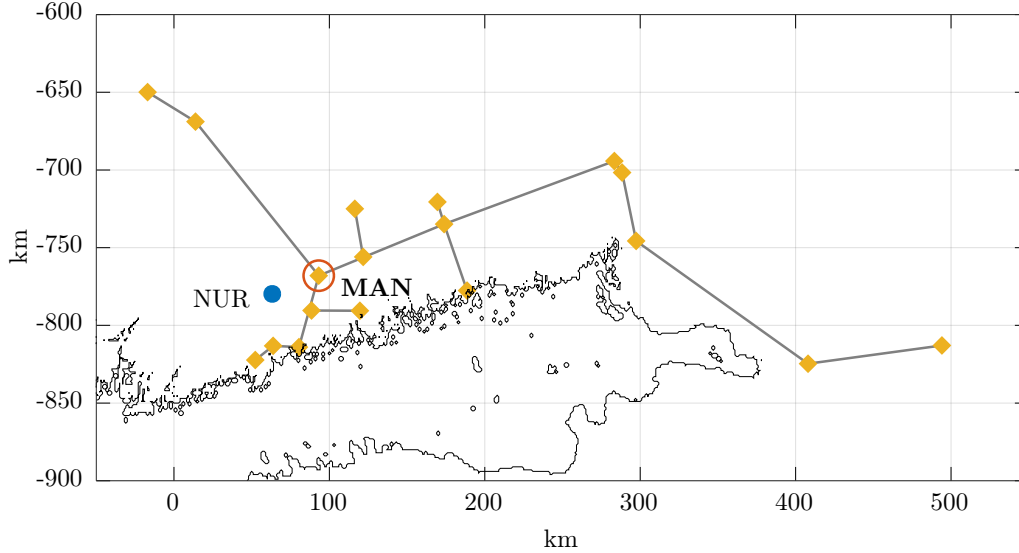


**Figure 5.** Geometry of the pipeline (grey lines) and location of 18 pipeline’s nodes and ends (gold diamonds); Mäntsälä (MAN) natural gas pipeline recording point (open red circle). For reference, the location of the IMAGE observatory, Nurmijärvi (NUR; blue-filled circle) is shown.

289 (TF) concept where MS TF relate the GEF at any location with horizontal magnetic  
 290 field at (fixed) multiple locations.

291 Using Fennoscandia as an example region and the SECS method to derive the spa-  
 292 tial modes, we compared the observed time series of the GEF and GIC available in the  
 293 region with those simulated using the proposed approach. Good agreement between ob-  
 294 served and modeled results validates the methodology. Notably, in contrast to the pre-  
 295 vious study (Marshalko et al., 2023), where GIC was calculated using the GEF at the  
 296 pipeline node where GIC is measured, in this paper, we considered a more realistic sce-  
 297 nario when GIC is calculated using simulated GEF at multiple nodes of the actual pipeline  
 298 grid.

299 While the simulations of GICs in this paper are mainly done for validation purposes,  
 300 the presented approach opens an avenue to derive a GIC activity indicator. Combining (6)  
 301 and (15) one can estimate GIC in real time. Moreover, as demonstrated in this paper,  
 302 the estimated GIC values correspond very accurately to the true recordings for a par-  
 303 ticular period when the conductor network can be assumed to be unchanged. Outside  
 304 of this period, the resulting GIC provides a meaningful proxy. Although it may not any  
 305 more give the true current, it can still be compared to other events in a relative sense.  
 306 For example, in our case, we could use the Halloween storm as a benchmark. Thus this  
 307 method has an immediate potential to be implemented as an operative product for space  
 308 weather services.

309 The prerequisite for the method’s application is continuous magnetic field measure-  
 310 ments at multiple locations, as in Fennoscandia. North America and China (with exist-  
 311 ing networks of magnetic field observations), or/and New Zealand (with the network of  
 312 variometers is being established now) are regions where the proposed method is worth  
 313 trying.

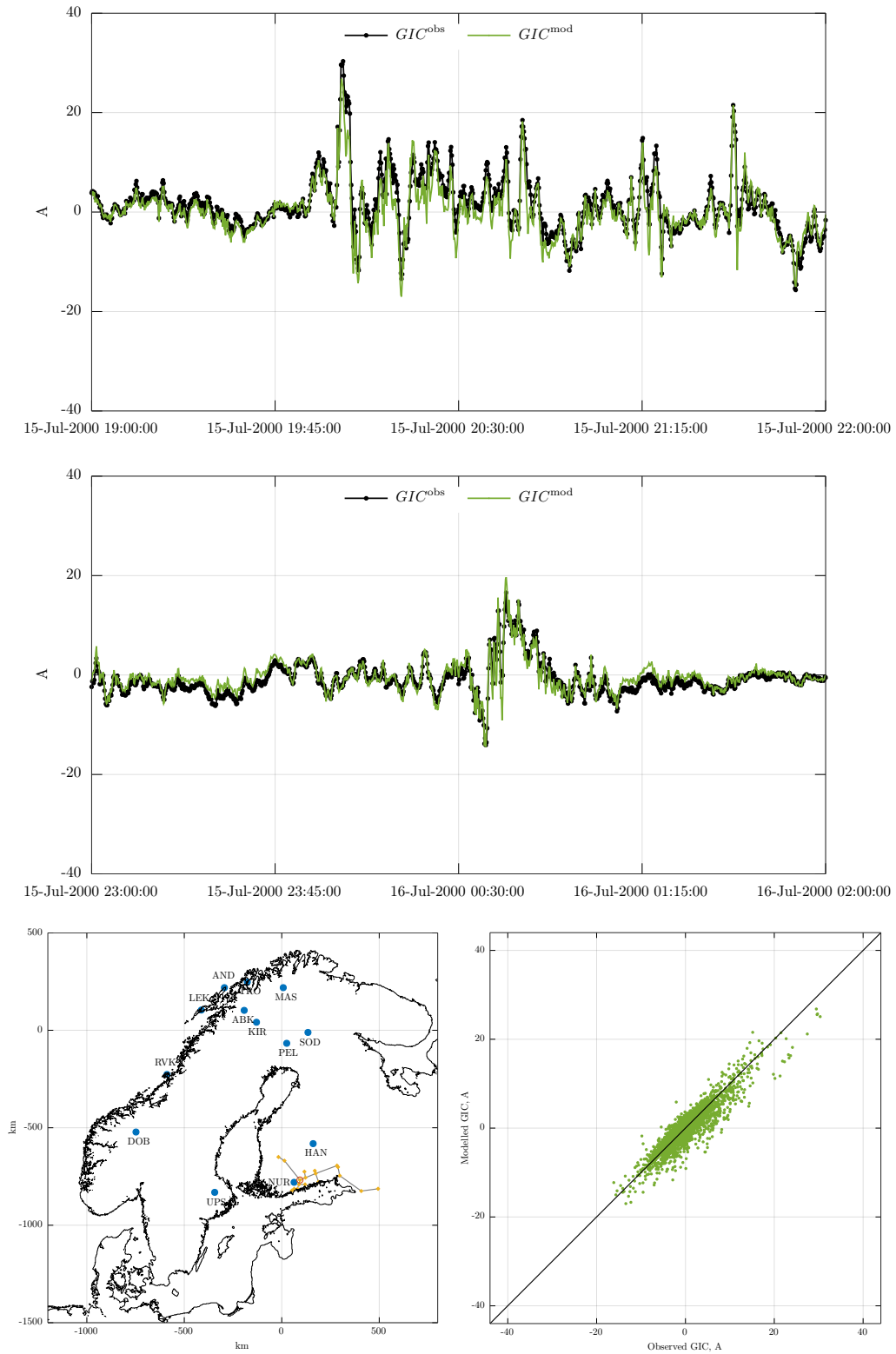


**Figure 6.** Substorms of 15/16 July 2000. Top two panels: comparison of observed and modeled GIC for two 3-hour time intervals. Bottom left panel: location of 13 IMAGE sites (blue-filled circles) used for the GEF simulation. Bottom right panel: cross-plots of observed and modeled GIC (cross-plots are demonstrated for the 2-day time interval: July 15 – 16 2000).

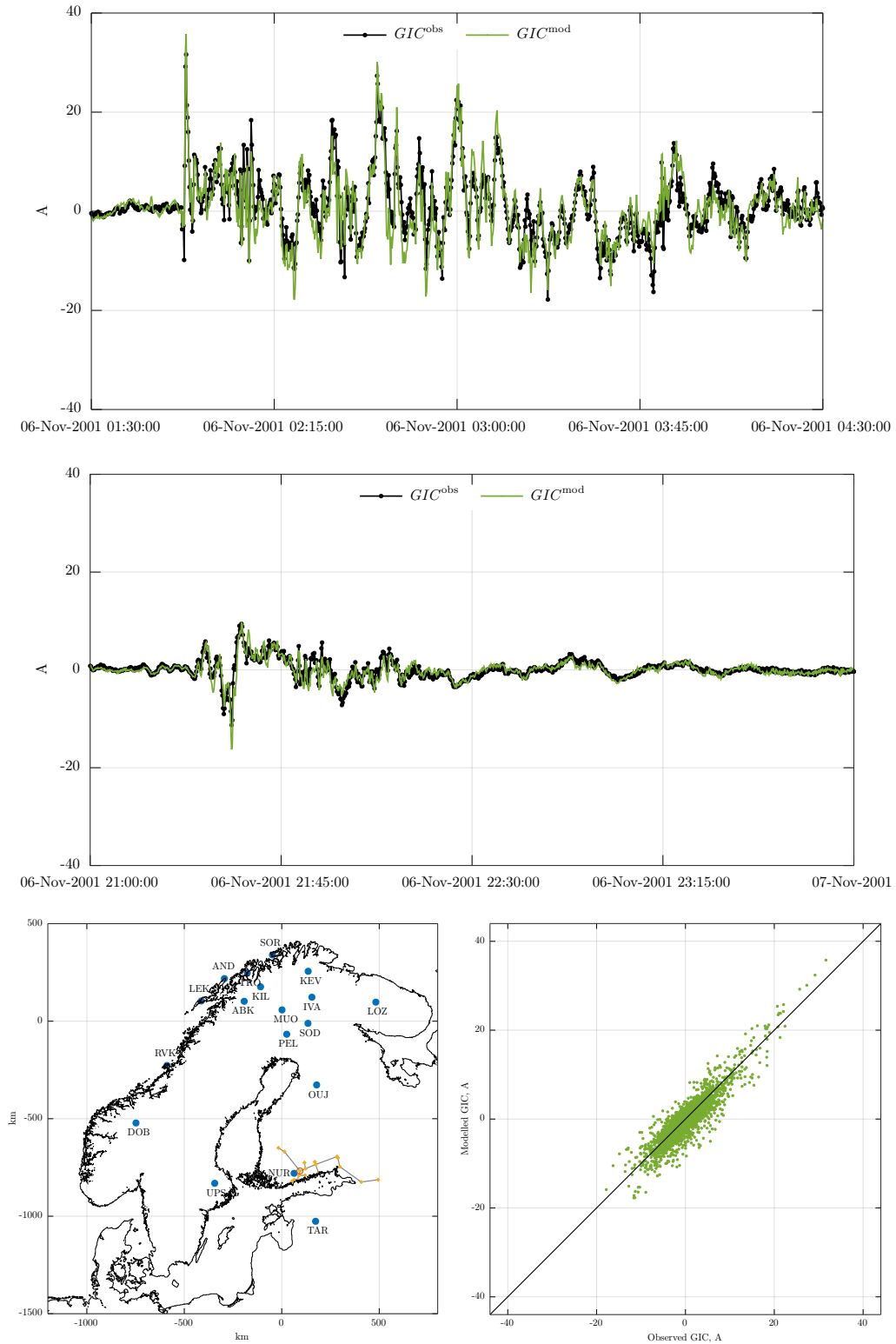


**Figure 7.** Substorms of 6 November 2001. Top two panels: comparison of observed and modeled GIC for two 3-hour time intervals. Bottom left panel: location of 18 IMAGE sites (blue-filled circles) used for the GEF simulation. Bottom right panel: cross-plots of observed and modeled GIC (cross-plots are demonstrated for the 2-day time interval: November 5 – 6 2001).

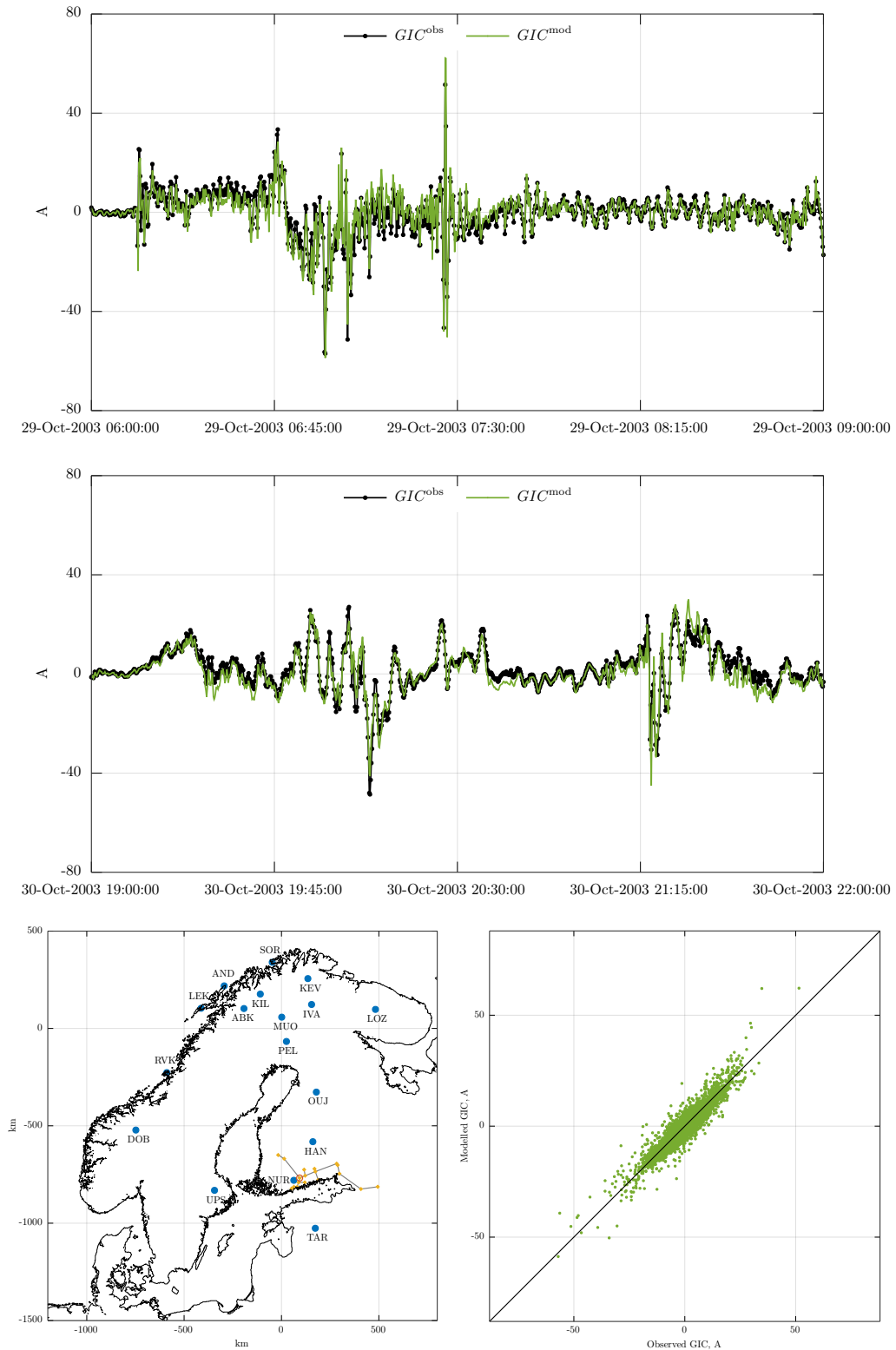


**Figure 8.** Substorms of 29/30 October 2003. Top two panels: comparison of observed and modeled GIC for two 3-hour time intervals. Bottom left panel: location of 17 IMAGE sites (blue-filled circles) used for the GEF simulation. Bottom right panel: cross-plots of observed and modeled GIC (cross-plots are demonstrated for the 3-day time interval: October 29 – November 1 2003).

314 It is worth noting that while comparing measured and simulated GEF at two se-  
 315 lected sites separated by only 21 km, we observe that experimental GEF at these sites  
 316 differ more significantly than the modeled GEF. Bearing in mind that the inducing source  
 317 (equivalent ionospheric current) is relatively (spatially) smooth, the most probable rea-  
 318 son for substantial lateral variability of the experimental GEF is local sharp lateral gra-  
 319 dients of the subsurface conductivity not accounted for in the used 3-D conductivity model  
 320 of the region. This prompts building a new – more accurate and detailed – 3-D conduc-  
 321 tivity model of Fennoscandia via a multi-scale 3-D inversion (using new modern inverse  
 322 solvers) of both old data (on which SMAP model was based) and a large amount of new  
 323 MT data collected in the region in the framework of various MT projects.

324 Finally, we have to mention that the proposed concept of multi-site transfer func-  
 325 tions can be easily adapted to another space weather related problem – accounting for  
 326 the geomagnetic disturbances during offshore directional drilling in northern seas (like  
 327 offshore of Alaska, Norway, British Isles, and North Russia), where magnetic field vari-  
 328 ations are routinely recorded at multiple adjacent land-based locations. In this scenario,  
 329 MS TF will relate magnetic field variations at sea bottom with those at multiple land-  
 330 based sites.

## 331 6 Open Research

332 The SMAP model (Korja et al., 2002) is available at the European Plate Observ-  
 333 ing System (EPOS) portal via EPOS (2019) (stored in JSON format and compressed  
 334 with bzip2) under CC BY-NC 4.0. PGIEM2G 3-D EM forward modeling code is avail-  
 335 able at Kruglyakov (2022) under GPLv2. GIC data are available at the website of the  
 336 Space and Earth Observation Centre of the Finnish Meteorological Institute (FMI) via  
 337 FMI (2023) under CC BY 4.0.

## 338 Acknowledgments

339 MK was supported by the New Zealand Ministry of Business, Innovation, & Employ-  
 340 ment through Endeavour Fund Research Programme contract UOOX2002. AK and MK  
 341 were also partially supported in the framework of Swarm DISC activities, funded by ESA  
 342 contract no. 4000109587, with support from EO Science for Society. EM and AV were  
 343 supported by grants 339329 from the Academy of Finland. We thank the institutes that  
 344 maintain the IMAGE Magnetometer Array: Tromsø Geophysical Observatory of UiT,  
 345 the Arctic University of Norway (Norway), Finnish Meteorological Institute (Finland),  
 346 Institute of Geophysics Polish Academy of Sciences (Poland), GFZ German Research Cen-  
 347 ter for Geosciences (Germany), Geological Survey of Sweden (Sweden), Swedish Insti-  
 348 tute of Space Physics (Sweden), Sodankylä Geophysical Observatory of the University  
 349 of Oulu (Finland), and Polar Geophysical Institute (Russia). We acknowledge Gasum  
 350 Oy for long-term collaboration in GIC studies of the Finnish natural gas pipeline.

## 351 References

- 352 Bailey, R., Halbedl, T. S., Schattauer, I., Achleitner, G., & Leonhardt, R. (2018).  
 353 Validating GIC models with measurements in Austria: Evaluation of accuracy  
 354 and sensitivity to input parameters. *Space Weather*, *16*(7), 887–902. doi:  
 355 10.1029/2018SW001842
- 356 Beggan, C. D. (2015). Sensitivity of geomagnetically induced currents to varying au-  
 357 roral electrojet and conductivity models. *Earth Planets Space*, *67*(24). doi: 10  
 358 .1186/s40623-014-0168-9
- 359 Beggan, C. D., Richardson, G. S., Baillie, O., Hübert, J., & Thomson, A. W. P.  
 360 (2021). Geoelectric field measurement, modelling and validation during  
 361 geomagnetic storms in the UK. *J. Space Weather Space Clim.*, *11*, 37.

- 362 <https://doi.org/10.1051/swsc/2021022> doi: 10.1051/swsc/2021022
- 363 Boteler, D. H. (2013, 01). A new versatile method for modelling geomagnetic induction  
364 in pipelines. *Geophysical Journal International*, *193*(1), 98-109. <https://doi.org/10.1093/gji/ggs113> doi: 10.1093/gji/ggs113
- 365 Boteler, D. H., & Pirjola, R. J. (2014). Comparison of methods for modelling  
366 geomagnetically induced currents. *Annales Geophysicae*, *32*(9), 1177–  
367 1187. <https://angeo.copernicus.org/articles/32/1177/2014/> doi:  
368 10.5194/angeo-32-1177-2014
- 369  
370 Campanyà, J., Gallagher, P. T., Blake, S. P., Gibbs, M., Jackson, D., Beggan,  
371 C. D., ... Hogg, C. (2019). Modeling geoelectric fields in Ireland and the  
372 UK for space weather applications. *Space Weather*, *17*(2), 216-237. <https://agupubs.onlinelibrary.wiley.com/doi/abs/10.1029/2018SW001999> doi:  
373 <https://doi.org/10.1029/2018SW001999>
- 374  
375 Dimmock, A. P., Rosenqvist, L., Hall, J.-O., Viljanen, A., Yordanova, E., Honko-  
376 nen, I., ... Sjöberg, E. C. (2019). The GIC and geomagnetic response over  
377 Fennoscandia to the 7-8 September 2017 geomagnetic storm. *Space Weather*,  
378 *17*(7), 989–1010. doi: 10.1029/2018SW002132
- 379 Divett, T., Ingham, M., Beggan, C. D., Richardson, G. S., Rodger, C. J., Thomson,  
380 A. W. P., & Dalzell, M. (2017). Modeling geoelectric fields and geomag-  
381 netically induced currents around New Zealand to explore GIC in the South  
382 Island's electrical transmission network. *Space Weather*, *15*(10), 1396–1412.  
383 doi: 10.1002/2017SW001697
- 384 Divett, T., Mac Manus, D. H., Richardson, G. S., Beggan, C. D., Rodger, C. J.,  
385 Ingham, M., ... Obana, Y. (2020). Geomagnetically induced current  
386 model validation from New Zealand's South Island. *Space Weather*, *18*(8),  
387 e2020SW002494. doi: 10.1029/2020SW002494
- 388 EPOS. (2019). *Dataset for "Crustal conductivity in Fennoscandia – a compilation of*  
389 *a database on crustal conductance in the Fennoscandian Shield"*, Korja et al.,  
390 2002, *Earth, Planets and Space* [Dataset]. European Plate Observing System  
391 (EPOS). [https://mt.research.ltu.se/MT/BEAR/1998/BEAR\\_3D.mod.json](https://mt.research.ltu.se/MT/BEAR/1998/BEAR_3D.mod.json)
- 392 FMI. (2023). *GIC recordings in the Finnish natural gas pipeline - ASCII files*  
393 [Dataset]. Finnish Meteorological Institute (FMI). [https://space.fmi.fi/gic/man\\_ascii/man.php](https://space.fmi.fi/gic/man_ascii/man.php)
- 394  
395 Honkonen, I., Kuvshinov, A., Rastätter, L., & Pulkkinen, A. (2018). Predicting  
396 global ground geoelectric field with coupled geospace and three-dimensional  
397 geomagnetic induction models. *Space Weather*, *16*(8), 1028–1041. doi:  
398 10.1029/2018SW001859
- 399 Jiracek, G. R. (1990). Near-surface and topographic distortions in electromagnetic  
400 induction. *Surv. Geophys.*, *11*, 163-203.
- 401 Kelbert, A., Balch, C., Pulkkinen, A., Egbert, G., Love, J., Rigler, J., & Fujii, I.  
402 (2017). Methodology for time-domain estimation of storm time geoelectric  
403 fields using the 3-D magnetotelluric response tensors. *Space Weather*, *15*(7),  
404 874–894. doi: doi:10.1002/2017SW001594
- 405 Korja, T., Engels, M., Zhamaletdinov, A. A., Kovtun, A. A., Palshin, N. A.,  
406 Smirnov, M. Y., ... BEAR Working Group (2002). Crustal conductiv-  
407 ity in Fennoscandia – a compilation of a database on crustal conductance  
408 in the Fennoscandian Shield. *Earth, Planets and Space*, *54*, 535–558. doi:  
409 10.1186/BF03353044
- 410 Kruglyakov, M. (2022). *PGIEM2G* [Software]. Gitlab. [https://gitlab.com/m](https://gitlab.com/m.kruglyakov/PGIEM2G)  
411 [.kruglyakov/PGIEM2G](https://gitlab.com/m.kruglyakov/PGIEM2G)
- 412 Kruglyakov, M., & Kuvshinov, A. (2018). Using high-order polynomial basis in 3-D  
413 EM forward modeling based on volume integral equation method. *Geophysical*  
414 *Journal International*, *213*(2), 1387–1401. doi: 10.1093/gji/ggy059
- 415 Kruglyakov, M., Kuvshinov, A., & Marshalko, E. (2022). Real-time 3-D modeling of  
416 the ground electric field due to space weather events. A concept and its valida-

- 417 tion. *Space Weather*, 20(4), e2021SW002906. doi: 10.1029/2021SW002906
- 418 Kruglyakov, M., Kuvshinov, A., & Nair, M. (2022). A proper use of the adja-  
 419 cent land-based observatory magnetic field data to account for the geomag-  
 420 netic disturbances during offshore directional drilling. *Space Weather*. doi:  
 421 10.1029/2022SW003238
- 422 Kuvshinov, A., Grayver, A., Tøffner-Clausen, L., & Olsen, N. (2021). Probing 3-D  
 423 electrical conductivity of the mantle using 6 years of Swarm, CryoSat-2 and  
 424 observatory magnetic data and exploiting matrix Q-responses approach. *Earth,*  
 425 *Planets and Space*, 73, 67. doi: 10.1186/s40623-020-01341-9
- 426 Malone-Leigh, J., Companyà, J., Gallagher, P. T., Neukirch, M., Hogg, C., &  
 427 Hodson, J. (2023). Nowcasting geoelectric fields in Ireland using mag-  
 428 netotelluric transfer functions. *J. Space Weather Space Clim.*, 13, 6.  
 429 <https://doi.org/10.1051/swsc/2023004> doi: 10.1051/swsc/2023004
- 430 Marshalko, E., Kruglyakov, M., Kuvshinov, A., Juusola, L., Kwagala, N. K.,  
 431 Sokolova, E., & Pilipenko, V. (2021). Comparing three approaches to  
 432 the inducing source setting for the ground electromagnetic field modeling  
 433 due to space weather events. *Space Weather*, 19(2), e2020SW002657. doi:  
 434 10.1029/2020SW002657
- 435 Marshalko, E., Kruglyakov, M., Kuvshinov, A., Murphy, B. S., Rastätter, L.,  
 436 Ngwira, C., & Pulkkinen, A. (2020). Exploring the influence of lateral  
 437 conductivity contrasts on the storm time behavior of the ground electric  
 438 field in the eastern United States. *Space Weather*, 18(2), 159–195. doi:  
 439 10.1029/2019SW002216
- 440 Marshalko, E., Kruglyakov, M., Kuvshinov, A., & Viljanen, A. (2023). Rigorous  
 441 3-D modeling of the ground electric field in Fennoscandia during the Halloween  
 442 geomagnetic storm. *Space Weather, revision submitted. Preprint at ESS Open*  
 443 *Archive. DOI: 10.22541/essoar.167631318.88816433/v2.*
- 444 Marshall, R. A., Dalzell, M., Waters, C. L., Goldthorpe, P., & Smith, E. A. (2012).  
 445 Geomagnetically induced currents in the new zealand power network. *Space*  
 446 *Weather*, 10(8). [https://agupubs.onlinelibrary.wiley.com/doi/abs/](https://agupubs.onlinelibrary.wiley.com/doi/abs/10.1029/2012SW000806)  
 447 [10.1029/2012SW000806](https://doi.org/10.1029/2012SW000806) doi: <https://doi.org/10.1029/2012SW000806>
- 448 Marshall, R. A., Wang, L., Paskos, G. A., Olivares-Pulido, G., Van Der Walt, T.,  
 449 Ong, C., ... Yoshikawa, A. (2019). Modeling geomagnetically induced cur-  
 450 rents in Australian power networks using different conductivity models. *Space*  
 451 *Weather*, 17(5), 727–756. doi: <https://doi.org/10.1029/2018SW002047>
- 452 Nakamura, S., Ebihara, Y., Fujita, S., Goto, T., Yamada, N., Watari, S., &  
 453 Omura, Y. (2018). Time domain simulation of geomagnetically induced  
 454 current (GIC) flowing in 500-kv power grid in Japan including a three-  
 455 dimensional ground inhomogeneity. *Space Weather*, 16(12), 1946–1959. doi:  
 456 10.1029/2018SW002004
- 457 Pulkkinen, A., Lindahl, S., Viljanen, A., & Pirjola, R. (2005). Geomagnetic storm  
 458 of 29–31 October 2003: Geomagnetically induced currents and their relation  
 459 to problems in the Swedish high-voltage power transmission system. *Space*  
 460 *Weather*, 3(8), S08C03. doi: 10.1029/2004SW000123
- 461 Pulkkinen, A., Viljanen, A., Pajunpää, K., & Pirjola, R. (2001). Recordings  
 462 and occurrence of geomagnetically induced currents in the Finnish natural  
 463 gas pipeline network. *Journal of Applied Geophysics*, 48(4), 219–231. doi:  
 464 10.1016/S0926-9851(01)00108-2
- 465 Püthe, C., Manoj, C., & Kuvshinov, A. (2014). Reproducing electric field ob-  
 466 servations during magnetic storms by means of rigorous 3-D modelling and  
 467 distortion matrix co-estimation. *Earth, Planets and Space*, 66, 162–171.
- 468 Rodger, C. J., Mac Manus, D. H., Dalzell, M., Thomson, A. W. P., Clarke, E.,  
 469 Petersen, T., ... Divett, T. (2017). Long-term geomagnetically induced  
 470 current observations from new zealand: Peak current estimates for ex-  
 471 treme geomagnetic storms. *Space Weather*, 15(11), 1447–1460. <https://>

- 472 agupubs.onlinelibrary.wiley.com/doi/abs/10.1002/2017SW001691 doi:  
473 https://doi.org/10.1002/2017SW001691
- 474 Rosenqvist, L., & Hall, J. O. (2019). Regional 3-D modeling and verification of ge-  
475 omagnetically induced currents in Sweden. *Space Weather*, *17*(1), 27–36. doi:  
476 10.1029/2018SW002084
- 477 Smirnov, M., Korja, T., & Pedersen, L. (2006). Electromagnetic Mini Array  
478 (EMMA) Project in Fennoscandia Looking into Deep Lithosphere. In *Pro-*  
479 *ceedings of the 7th International Conference: PROBLEMS OF GEOCOSMOS,*  
480 *St. Petersburg.*
- 481 Tanskanen, E. I. (2009). A comprehensive high-throughput analysis of substorms ob-  
482 served by IMAGE magnetometer network: Years 1993–2003 examined. *J. Geo-*  
483 *phys. Res.*, *114*(A5). doi: 10.1029/2008JA013682
- 484 Trichtchenko, L., & Boteler, D. H. (2002). Modelling of geomagnetic induc-  
485 tion in pipelines. *Annales Geophysicae*, *20*(7), 1063–1072. [https://](https://angeo.copernicus.org/articles/20/1063/2002/)  
486 [angeo.copernicus.org/articles/20/1063/2002/](https://angeo.copernicus.org/articles/20/1063/2002/) doi: 10.5194/angeo-20  
487 -1063-2002
- 488 Vanhamäki, H., & Juusola, L. (2020). Introduction to Spherical Elementary Current  
489 Systems. In M. W. Dunlop & H. Lühr (Eds.), *Ionospheric multi-spacecraft*  
490 *analysis tools: Approaches for deriving ionospheric parameters* (pp. 5–33).  
491 Cham: Springer International Publishing. doi: 10.1007/978-3-030-26732-2\_2
- 492 Viljanen, A., & Pirjola, R. (1994). Geomagnetically induced currents in the Finnish  
493 high-voltage power system. A geophysical review. *Surv. Geophys.*, *15*, 383–408.  
494 doi: 10.1007/BF00665999
- 495 Viljanen, A., Pirjola, R., Wik, M., Ádám, A., Prácsér, E., Sakharov, Y., & Katkalov,  
496 J. (2012). Continental scale modelling of geomagnetically induced currents. *J.*  
497 *Space Weather Space Clim.*, *2*, A17. doi: 10.1051/swsc/2012017
- 498 Viljanen, A., Pulkkinen, A., Pirjola, R., Pajunpää, K., Posio, P., & Koistinen, A.  
499 (2006). Recordings of geomagnetically induced currents and a nowcasting ser-  
500 vice of the Finnish natural gas pipeline system. *Space Weather*, *4*(10). doi:  
501 10.1029/2006SW000234
- 502 Wang, L., Lewis, A. M., Ogawa, Y., Jones, W. V., & Costelloe, M. T. (2016). Mod-  
503 eling geomagnetic induction hazards using a 3-D electrical conductivity model  
504 of Australia. *Space Weather*, *14*, 1125–1135. doi: 10.1002/2016SW001436
- 505 Wawrzaszek, A., Gil, A., Modzelewska, R., Tsurutani, B. T., & Wawrzaszek, R.  
506 (2023). Analysis of large geomagnetically induced currents during the 7–8  
507 september 2017 storm: Geoelectric field mapping. *Space Weather*, *21*(3),  
508 e2022SW003383. doi: <https://doi.org/10.1029/2022SW003383>

1 **Multi-site transfer function approach for real-time**  
2 **modeling of the ground electric field induced by**  
3 **laterally-nonuniform ionospheric source**

4 **Mikhail Kruglyakov<sup>1,2</sup>, Elena Marshalko<sup>3</sup>, Alexey Kuvshinov<sup>2</sup>, Maxim**  
5 **Smirnov<sup>4</sup>, and Ari Viljanen<sup>3</sup>**

6 <sup>1</sup>University of Otago, Dunedin, New Zealand

7 <sup>2</sup>Institute of Geophysics, ETH Zürich, Zürich, Switzerland

8 <sup>3</sup>Finnish Meteorological Institute, Helsinki, Finland

9 <sup>4</sup>Lulea University of Technology, Lulea, Sweden

10 **Key Points:**

- 11 • Multi-site transfer function approach is proposed for real-time modeling of the ground  
12 electric field induced by laterally-nonuniform source  
13 • The approach exploits magnetic field data from multiple locations and spatial modes  
14 describing the ionospheric source  
15 • Good agreement between modeled and observed GEF and GIC is demonstrated

---

Corresponding author: Mikhail Kruglyakov, [mikhail.kruglyakov@otago.ac.nz](mailto:mikhail.kruglyakov@otago.ac.nz)

## Abstract

We propose a novel approach to model the ground electric field (GEF) induced by laterally-nonuniform ionospheric sources in the real-time. The approach exploits the multi-site transfer function concept, continuous magnetic field measurements at multiple sites in the region of interest, and spatial modes describing the ionospheric source. We compared the modeled GEFs with those measured at two locations in Fennoscandia and observed good agreement between modeled and measured GEF. Besides, we compared GEF-based geomagnetically induced current (GIC) with that measured at the Mäntsälä natural gas pipeline recording point and again observed remarkable agreement between modeled and measured GIC.

## Plain Language Summary

The Earth’s magnetic field disturbances, like geomagnetic storms and magnetospheric substorms, generate geomagnetically induced currents (GIC) in technological systems like power grids. GIC calculation is of practical interest since, in some cases, GIC can cause power grid blackouts. An accurate GIC calculation, preferably in real-time, requires knowledge of the ground electric field (GEF) along power lines. The GEF is rarely measured directly, so it needs to be simulated using, as realistic as possible, models of the Earth’s electrical conductivity and the source responsible for geomagnetic disturbances. This study presents and validates a novel approach to model the GEF in real-time, which exploits – in a non-conventional way – magnetic field measurements at multiple sites in the region of interest.

## 1 Introduction

According to Faraday’s law, the large fluctuations of the Earth’s magnetic field during geomagnetic storms and magnetospheric substorms generate the ground electric field (GEF), which in turn drives the so-called geomagnetically induced currents (GIC) in ground-based technological systems, such as power grids and pipelines (Viljanen & Pirjola, 1994). GIC calculation is of practical interest since, in the worst case, GIC can cause the transformers’ destructions lead to power grid blackouts, as it happened, for example, in the Malmö region in Sweden on 30 October 2003 (Pulkkinen et al., 2005) and in Otago region in New Zealand on 6 November 2001 (Marshall et al., 2012; Rodger et al., 2017). An accurate calculation of GIC variations, ideally in real-time, requires knowledge of the spatio-temporal evolution of ground electric field (GEF) along power/pipelines. However, GEF measurements are occasional and, if they exist, usually last a few months at most. So the only alternative is the numerical simulation of the GEF.

The majority of the studies in connection with GEF or GIC simulations are based on the simplest model of the source, i.e. the laterally uniform one, and, often, but not always, on the laterally uniform conductivity distribution model (e.g. Wang et al. (2016); Divett et al. (2017); Kelbert et al. (2017); Bailey et al. (2018); Nakamura et al. (2018); Marshall et al. (2019); Rosenqvist and Hall (2019); Divett et al. (2020)). The intermediate approach for the use of a non-uniform source without the full simulations for one is used in (Viljanen et al., 2012), (Campanyà et al., 2019) and (Malone-Leigh et al., 2023), where the relations between electric and magnetic fields are based on plane-wave assumption, while the magnetic field is obtained by the interpolation from few observation sites. As for the full simulations with non-uniform sources, there are just a few of them (e.g. Beggan (2015); Honkonen et al. (2018); Marshalko et al. (2020, 2021); Beggan et al. (2021)).

Very recently Kruglyakov, Kuvshinov, and Marshalko (2022) proposed a method for real-time modeling of the GEF induced by laterally-varying ionospheric sources. Their technique is based on the isolation of the inducing source (approximated by ionospheric sheet current) using the Spherical Elementary Current System (SECS) approach (Vanhamäki

65 & Juusola, 2020) as applied to the magnetic field variations simultaneously recorded at  
 66 a regional network of observations. Further, the source is factorized by spatial modes (SM)  
 67 and respective time-varying expansion coefficients using time-domain Principal Compo-  
 68 nent Analysis (PCA) of SECS-recovered inducing current.

69 The SECS approach can be viewed as a regional variant of the Gauss method —  
 70 the method used to separate the inducing and induced signals on a global scale. If the  
 71 region of interest is characterized by 3-D conductivity distribution, the induced part is  
 72 inevitably influenced by 3-D effects arising, particularly from the lateral (for example,  
 73 land/ocean) conductivity contrasts. Given the usually deficient spatial distribution of  
 74 the magnetic field observations, the SECS approach precludes an accurate description  
 75 of the induced part affected by localized 3-D effects. Such imperfection in the induced  
 76 part description also influences the recovery of the inducing part in terms of the recovery  
 77 of the time series of expansion coefficients.

78 To circumvent this problem Marshalko et al. (2023) introduced an approach to es-  
 79 timate expansion coefficients more accurately. The approach also exploits the spatial modes  
 80 resulting from the PCA of SECS-recovered inducing source, but an estimation of the ex-  
 81 pansion coefficients is performed using a 3-D conductivity model of the region. However,  
 82 the disadvantage of their method is a high computational load to obtain expansion co-  
 83 efficients, thus precluding its implementation for real-time GEF modeling.

84 This paper proposes a method that also works with spatial modes but avoids es-  
 85 timating the expansion coefficients. An approach is based on the multi-site (MS) trans-  
 86 fer function (TF) concept where MS TF relate the GEF at any location with a horizon-  
 87 tal components of magnetic field at (fixed) multiple locations. Notably, an approach al-  
 88 lows researchers to model the GEF in real time. The proposed technique can be consid-  
 89 ered a generalization of the inter-site TF formalism presented in (Kruglyakov, Kuvshi-  
 90 nov, & Nair, 2022). In their paper, TFs relate sea-bed and single-site land-based mag-  
 91 netic fields, and spatial modes are obtained from spherical harmonic analysis of the mag-  
 92 netic data recorded at a global network of geomagnetic observatories.

93 Using Fennoscandia as a study region, we validate the MS TF approach by compar-  
 94 ing modeled and measured GEF and GIC time series. The reasons for selecting this  
 95 high-latitude region are manifold. First, technological systems in polar regions are es-  
 96 pecially vulnerable due to the excessive GIC. Second, the inducing source at high lat-  
 97 itudes reveals significant lateral variability, which we are interested in accounting for in  
 98 our approach. Third, the 3-D electrical conductivity model is available for Fennoscan-  
 99 dia (Korja et al., 2002). Fourth, there is a magnetometer network in the region (Inter-  
 100 national Monitor for Auroral Geomagnetic Effect, IMAGE (Tanskanen, 2009)), which  
 101 provides long-term, simultaneous and continuous measurements of the magnetic field at  
 102 multiple locations — the prerequisite data for successfully applying the proposed approach.  
 103 Moreover, in Fennoscandia, one can find relatively long (from weeks to months) contin-  
 104 uous GEF measurements performed during magnetotelluric surveys in the region. Fi-  
 105 nally, GIC observations have been carried out at the Mäntsälä natural gas pipeline record-  
 106 ing point starting from November 1998 (Viljanen et al., 2006), allowing us to compare  
 107 observed and modeled GIC for several space weather events.

## 108 2 Methodology

We assume that the horizontal ground electric field  $\mathbf{E}_h = (E_x, E_y)$  at any loca-  
 tion is related in the frequency domain to  $\mathbf{B}_h = (B_x, B_y)$  at  $N$  sites as

$$\mathbf{E}_h(\mathbf{r}, \omega; \sigma) = \sum_{k=1}^N \Lambda(\mathbf{r}, \mathbf{r}_k, \omega; \sigma) \mathbf{B}_h(\mathbf{r}_k, \omega; \sigma), \quad (1)$$

109 where  $x$  and  $y$  are directed to geographic North and East, respectively.

A set of  $\Lambda_k \equiv \Lambda(\mathbf{r}, \mathbf{r}_k, \omega; \sigma)$  is called multi-site transfer function, where each  $\Lambda_k$  is the following  $2 \times 2$  matrix

$$\Lambda_k = \begin{pmatrix} \Lambda_{xx,k} & \Lambda_{xy,k} \\ \Lambda_{yx,k} & \Lambda_{yy,k} \end{pmatrix}. \quad (2)$$

Estimating the elements of matrices  $\Lambda_k$ ,  $k = 1, 2, \dots, N$  at a given frequency  $\omega$  and conductivity model  $\sigma$  is performed as follows. First, one calculates the fields  $\mathbf{B}^{(l)}(\mathbf{r}_k, \omega; \sigma)$  and  $\mathbf{E}^{(l)}(\mathbf{r}, \omega; \sigma)$  corresponding to  $l$ -th spatial modes  $\mathbf{j}_l(\mathbf{r})$  describing the inducing (extraneous) source

$$\mathbf{j}^{\text{ext}}(\mathbf{r}, t) = \sum_{l=1}^L c_l(t) \mathbf{j}_l(\mathbf{r}), \quad (3)$$

where  $L$  stands for a number of spatial modes. Then the elements of  $\Lambda_k$  are estimated row-wise using the calculated  $\mathbf{B}_h^{(l)}$  and  $\mathbf{E}_h^{(l)}$  fields. Specifically, elements of  $\Lambda_k$  are obtained as the solution of the following two systems of linear equations (SLE)

$$\Lambda_{xx,1} B_x^{(l)}(\mathbf{r}_1) + \Lambda_{xy,1} B_y^{(l)}(\mathbf{r}_1) + \dots + \Lambda_{xx,N} B_x^{(l)}(\mathbf{r}_N) + \Lambda_{xy,N} B_y^{(l)}(\mathbf{r}_N) = E_x^{(l)}(\mathbf{r}), \quad (4)$$

and

$$\Lambda_{yx,1} B_x^{(l)}(\mathbf{r}_1) + \Lambda_{yy,1} B_y^{(l)}(\mathbf{r}_1) + \dots + \Lambda_{yx,N} B_x^{(l)}(\mathbf{r}_N) + \Lambda_{yy,N} B_y^{(l)}(\mathbf{r}_N) = E_y^{(l)}(\mathbf{r}), \quad (5)$$

110 where  $l = 1, 2, \dots, L$ . Note, that in Equations (4) and (5) the dependency of all quan-  
 111 tities on  $\omega$ ,  $\mathbf{B}_h^{(l)}$  and  $\mathbf{E}_h^{(l)}$  on  $\sigma$ , and elements of  $\Lambda_k$  on  $\sigma$ ,  $\mathbf{r}$  and  $\mathbf{r}_k$  are omitted but im-  
 112 plied. To resolve the TF, the number of spatial modes,  $L$ , should be equal to or larger  
 113 than the doubled number of the sites,  $N$ , i.e.  $L \geq 2N$ . Also, our model experiments  
 114 indicate that the condition number of the system matrices in Equations (4) and (5) can  
 115 be quite large, so we used the regularized ordinary least squares approach to solve the  
 116 above SLEs.

Once elements of  $\Lambda_k$  are estimated at a predefined number of frequencies, the GEF at a given time instant  $t_i = i\Delta t$  and a given location  $\mathbf{r}$  is then calculated using a numerical scheme similar to that described by Marshalko et al. (2023)(cf. Equation 20 of that paper), namely

$$\mathbf{E}_h(\mathbf{r}, t_i; \sigma) = \sum_{n=0}^{N_t} \sum_{k=1}^N \Lambda^{(n)}(\mathbf{r}, \mathbf{r}_k, T_\Lambda; \sigma) \mathbf{B}_h^{\text{obs}}(\mathbf{r}_k, t_i - n\Delta t), \quad (6)$$

where  $\mathbf{B}_h^{\text{obs}}$  stands for horizontal components of the observed field in corresponding locations and  $N_t = T_\Lambda/\Delta t$ . As discussed in (Marshalko et al., 2023), computation of quantities like  $\Lambda^n(\mathbf{r}, \mathbf{r}_k, T_\Lambda; \sigma)$  can be reduced to the estimation of the following integrals

$$\Lambda^{(n)}(\mathbf{r}, \mathbf{r}_k, T_\Lambda; \sigma) = \text{Re} \left\{ \frac{\Delta t}{\pi} \int_0^{\frac{\pi}{\Delta t}} \Lambda(\mathbf{r}, \mathbf{r}_k, \omega; \sigma) e^{-i\omega n \Delta t} d\omega \right\}, \quad n = 1, 2, \dots, N_\Lambda - 1. \quad (7)$$

117 Expressions for  $\Lambda^{(0)}$  and  $\Lambda^{N_\Lambda}$  are more complicated, but their calculation is similar to  
 118 that presented in Appendix A of (Marshalko et al., 2023) to calculate the correspond-  
 119 ing terms for the electric field.

120 Computation of the integrals in Equation (7) is performed as follows. First,  $\Lambda(\mathbf{r}, \mathbf{r}_k, \omega; \sigma)$   
 121 are computed at  $N_f$  logarithmically spaced frequencies from  $f_{\min}$  to  $f_{\max}$  using Equations (4) and (5).  
 122 Further, one can analytically compute the corresponding integrals by exploiting cubic spline interpolation  
 123 as applied to calculated  $\Lambda$ . Our model experiments  
 124 (not shown in the paper) indicate that  $N_f = 71$ ,  $f_{\min} = 6.13 \cdot 10^{-7}$  Hz, and  $f_{\max} = 0.054$  Hz  
 125 provide an accurate estimation of the integrals, in the assumption that  $\Delta t$  is taken as 10 s.

As seen from Equations (4) and (5), the estimation of  $\Lambda(\mathbf{r}, \mathbf{r}_k, \omega; \sigma)$  requires specification of  $\mathbf{j}_l, l = 1, 2, \dots, L$ . The form of  $\mathbf{j}_l$  (and their number,  $L$ ) varies with the application. As discussed in Introduction, in this paper, we use spatial modes obtained by means of the time-domain Principal Component Analysis (PCA) of the SECS-recovered inducing source. The reader can find further details on the derivation of these modes in the next section.

As also seen from Equations (4) and (5) (and already mentioned before), the estimation of  $\Lambda(\mathbf{r}, \mathbf{r}_k, \omega; \sigma)$  implies computations of  $\mathbf{B}^{(l)}(\mathbf{r}_k, \omega; \sigma)$  and  $\mathbf{E}^{(l)}(\mathbf{r}, \omega; \sigma)$  in a given conductivity model  $\sigma$  of the region of interest. We performed these computations using the scalable 3-D EM forward modeling code PGIEM2G (Kruglyakov & Kuvshinov, 2018) based on a method of volume integral equation.

Worth noting that quantities  $\Lambda^{(n)}(\mathbf{r}, \mathbf{r}_k, T_\Lambda; \sigma), n = 0, 1, \dots, N_t$  are time-invariant, and for a given conductivity model are calculated only once, then stored and used when the calculation of  $\mathbf{E}_h(\mathbf{r}, t; \sigma)$  is required.

It is also important to note that the “memory”  $T_\Lambda$  can be taken as short as 15 min (at least for Fennoscandia – the region we have selected to validate the presented approach). Namely, a small value for  $T_\Lambda$  allows us to calculate  $\mathbf{E}_h(\mathbf{r}, t; \sigma)$  in real time, provided long-term continuous observations of the magnetic field,  $\mathbf{B}_h^{\text{obs}}$  are available at multiple locations. Further justification of  $T_\Lambda$  smallness is presented in the following two sections.

Ideally,  $\Lambda$  should relate the electric field with the magnetic field measured at as large as possible number of sites. However, there are usually gaps in the magnetic field data. At the same time, to apply the presented methodology, one needs to use continuous time series of magnetic field during the interval  $[t_i - T_\Lambda, t_i]$  to compute  $\mathbf{E}_h(\mathbf{r}, t_i; \sigma)$ . Thus one has to choose observatories accordingly to continuous data availability. However, one can use different (precomputed) sets of  $\Lambda$  for different time instances  $t_i$ . Combining this option with the short  $T_\Lambda$  means that the number of sites with magnetic field observations in use is always large enough to implement the proposed approach.

The final remark of this section is that if the spatial modes are just two polarizations of vertically indenting plane wave, then  $\Lambda$  degenerates to intersite impedance  $Z$ ; cf. Section 2.2 of (Marshalko et al., 2023).

## 3 Results

### 3.1 3-D conductivity model

One of the critical components required for as realistic as feasible GEF modeling is a trustworthy conductivity model of the Earth’s subsurface in the region of interest. The conductivity model of Fennoscandia we adopt comprises a 3-D part (upper 60 km below the surface of the Earth) and the 1-D part underneath taken as a corresponding piece (deeper than 60 km) of the 1-D profile from (Kuvshinov et al., 2021). As for the 3-D part, it is based on the SMAP model (Korja et al., 2002), covers the area of  $2550 \times 2550 \text{ km}^2$  and consists of three layers of laterally variable conductivity of 10, 20, and 30 km thicknesses. The lateral discretization of the model is  $512 \times 512$  cells, meaning that cells’ size is about  $5 \times 5 \text{ km}^2$ . Note that this model (of the same discretization) was also used in (Marshalko et al., 2021; Kruglyakov, Kuvshinov, & Marshalko, 2022; Marshalko et al., 2023). The interested reader can find details on the conductivity distribution in the model, for example, in (Kruglyakov, Kuvshinov, & Marshalko, 2022), cf. their Figure 7. Note also that for  $T_\Lambda$  calculations only observatories located in the area covered by this model are used, i.e. not all IMAGE observatories.

172

### 3.2 Deriving spatial modes

173

174

175

As mentioned in the Introduction, spatial modes  $\mathbf{j}_l(\mathbf{r})$  are obtained using the SECS method and their derivation involves the following two steps (Kruglyakov, Kuvshinov, & Marshalko, 2022):

176

177

178

179

180

181

182

183

1. Spherical Elementary Current Systems (SECS) method (Vanhamäki & Juusola, 2020) is applied to 29–31 October 2003 (Halloween storm) ten-second IMAGE magnetic field data to separate the inducing and induced current systems that are assumed to flow 90 km above the Earth’s surface and 1 m below the Earth’s surface, correspondingly. The data from all 26 magnetometers were used to perform the SECS analysis. The locations of IMAGE magnetometers in use are demonstrated in Figure 1. Note that IMAGE data for this 72-hour time interval contain several gaps; linear interpolation was applied to fill these gaps.

184

185

186

2. The time-domain PCA is applied to the SECS-recovered inducing source resulting in the desired  $\mathbf{j}_l(\mathbf{r}), l = 1, 2, \dots, L$ . With  $L = 34$ , we described 99.9% of the inducing source variability.

187

188

189

190

191

192

193

194

195

It is relevant to mention that later in the paper, we analyze the data from the Halloween storm and other space weather events. One can argue that  $\mathbf{j}_l$  obtained for a specific event could be non-adequate for other events. Kruglyakov, Kuvshinov, and Marshalko (2022) addressed this question and demonstrated that irrespective of the event (which corresponds to sources of different geometry), the spatial structure of these sources is well approximated by a finite number of  $\mathbf{j}_l$  obtained from the analysis of some specific event (in our case the Halloween storm). The prerequisite to getting an adequate set of  $\mathbf{j}_l$  is that the event for their estimation should be long enough and sufficiently energetically large and spatially complex.

196

### 3.3 Comparing modeled and observed GEF

197

198

199

200

201

202

203

204

205

206

207

208

209

210

211

212

213

214

215

216

217

218

219

220

Even though there are multiple locations in Fennoscandia where continuous ground electric field measurements were performed for relatively long time intervals (from weeks to months), our analysis of the available data reveals that most of the GEF observations were conducted during periods of relatively quiet geomagnetic activity. Note that the potentially hazardous GIC are flowing in the technological systems during geomagnetic disturbances like geomagnetic storms and magnetospheric substorms, making such space weather events of particular interest in the context of this study. Fortunately, continuous (one-second) GEF measurements performed in August 2005 – June 2006 at 8 of 13 sites around Joensuu, Finland, in the framework of Electromagnetic Mini Array (EMMA) Project (Smirnov et al., 2006) have successfully recorded prominent space weather event – magnetospheric substorm of 11 September 2005; during this event, amplitudes of the observed GEF in the region exceeded 2000 mV/km. We compare modeled and measured time series of the GEF during this event at two sites (denoted below as M02 and M05) where the largest GEF amplitudes were observed and where the data quality – in terms of absence of gaps, jumps, and electrodes’ drift – was the highest. The comparison is performed for the time interval from 05:15 UT to 6:15 UT. This interval includes a 30-min long event and 15-min long quiet periods before and after the event. During this time interval, 16 IMAGE observation sites delivered uninterrupted magnetic field recordings, and thus, only the data from these sites were used to calculate the GEF using Equation (6). Figure 2 shows the location of these IMAGE sites (blue circles) and two sites (red circles) with GEF recordings selected for comparison of the observed and modeled GEF. Since GEF measurements were performed in geomagnetic coordinates, we decided to compare observed and modeled GEF components in this coordinate system. Thus, in this section, the  $x$ - and  $y$ -components of the GEF are geomagnetic North and East compo-

221 nents, respectively. Besides, experimental 1-sec time series of the GEF were re-sampled  
 222 to a 10-sec time series to make them compatible with IMAGE magnetic field data.

It is important to note here that depending on location, the modeled GEF might still over- or underestimate the amplitudes of the actual GEF. This is due to galvanic effects, i.e. the build-up of electric charges along local near-surface heterogeneities (Jiracek, 1990) that cannot be included in the model. Galvanic effects are commonly accounted for with a  $2 \times 2$  real-valued time-independent – unique for each location – distortion matrix,  $D$ , which linearly relates observed  $\mathbf{E}_h^{\text{obs}}$  and modeled  $\mathbf{E}_h^{\text{mod}}$  electric fields as (Pütke et al., 2014)

$$\mathbf{E}_h^{\text{obs}}(\mathbf{r}, t) = D(\mathbf{r})\mathbf{E}_h^{\text{mod}}(\mathbf{r}, t), \quad D(\mathbf{r}) = \begin{pmatrix} D_{xx} & D_{xy} \\ D_{yx} & D_{yy} \end{pmatrix}. \quad (8)$$

Having observed and calculated GEF at many time instants and bearing in mind that  $D$  is time-independent, we can form highly over-determined SLE given by Equation (8) to estimate elements of  $D$  using the least-square method. Specifically, these elements are estimated row-wise as the solutions of the following two SLEs

$$D_{xx}E_x^{\text{mod}}(t_i) + D_{xy}E_y^{\text{mod}}(t_i) = E_x^{\text{obs}}(t_i), \quad (9)$$

and

$$D_{yx}E_x^{\text{mod}}(t_i) + D_{yy}E_y^{\text{mod}}(t_i) = E_y^{\text{obs}}(t_i), \quad (10)$$

223 where  $t_i$  runs multiple ( $K$ ) time instants. Note that the dependence of all quantities in  
 224 Equations (9) and (10) on  $\mathbf{r}$  is omitted but implied. To make the comparison as fair as  
 225 possible, we calculated distortion matrices using the data not from the time interval where  
 226 we compare the results (05:15 – 06:15 September 11) but using the data far before the  
 227 event, specifically, namely the data from one (whole; September 9) day, giving  $K = 24 \times$   
 228  $3600/10 = 8640$  equations to estimate respective two elements.

As stated in the previous section, the memory  $T_\Lambda$  can be taken as short as 15 min in Equation (6). To explore whether this is the case, we performed GEF calculations taking  $T_\Lambda$  as 15, 30, 60 and 90 min. Figures 3 and 4 compare observed and (corrected for the distortion) modeled  $E_x$  and  $E_y$ , respectively, at sites M02 and M05 for different values of  $T_\Lambda$ . Note that the corrected modeled GEF are calculated by reusing Equation (8), i.e., as

$$\mathbf{E}_h^{\text{mod,corr}}(\mathbf{r}, t) = D(\mathbf{r})\mathbf{E}_h^{\text{mod}}(\mathbf{r}, t), \quad (11)$$

229 where elements of  $D$  are obtained from the solution of the SLEs (9) and (10). As is seen,  
 230 the modeled results for all values of  $T_\Lambda$  are indistinguishably similar, meaning that  $T_\Lambda$   
 231 can be taken as 15 min. Tables 1 and 2 confirm this inference more quantitatively by  
 232 showing correlation coefficients and coefficients of determination at sites M02 and M05,  
 233 respectively, for the considered 1-hour time interval. One can see that both quantities  
 234 practically do not differ with respect to the value of  $T_\Lambda$ .

235 What is also noticeable from the tables is that the agreement between experimen-  
 236 tal and modeled GEF (in terms of both correlation coefficients and coefficients of deter-  
 237 mination) is better in the  $E_y$  component. This is most probably because the ionospheric  
 238 current (source) flows predominantly in the  $y$  direction, making GEF modeling in this  
 239 direction more accurate. Returning to Figures 3 and 4, we also observe that the exper-  
 240 imental GEF at selected sites separated by only 21 km significantly differ, more consid-  
 241 erably than the modeled GEF. The most probable reason for this is the existence of lo-  
 242 cal 3-D conductivity heterogeneities in this region which are not accounted for in the avail-  
 243 able 3-D conductivity model of the region.

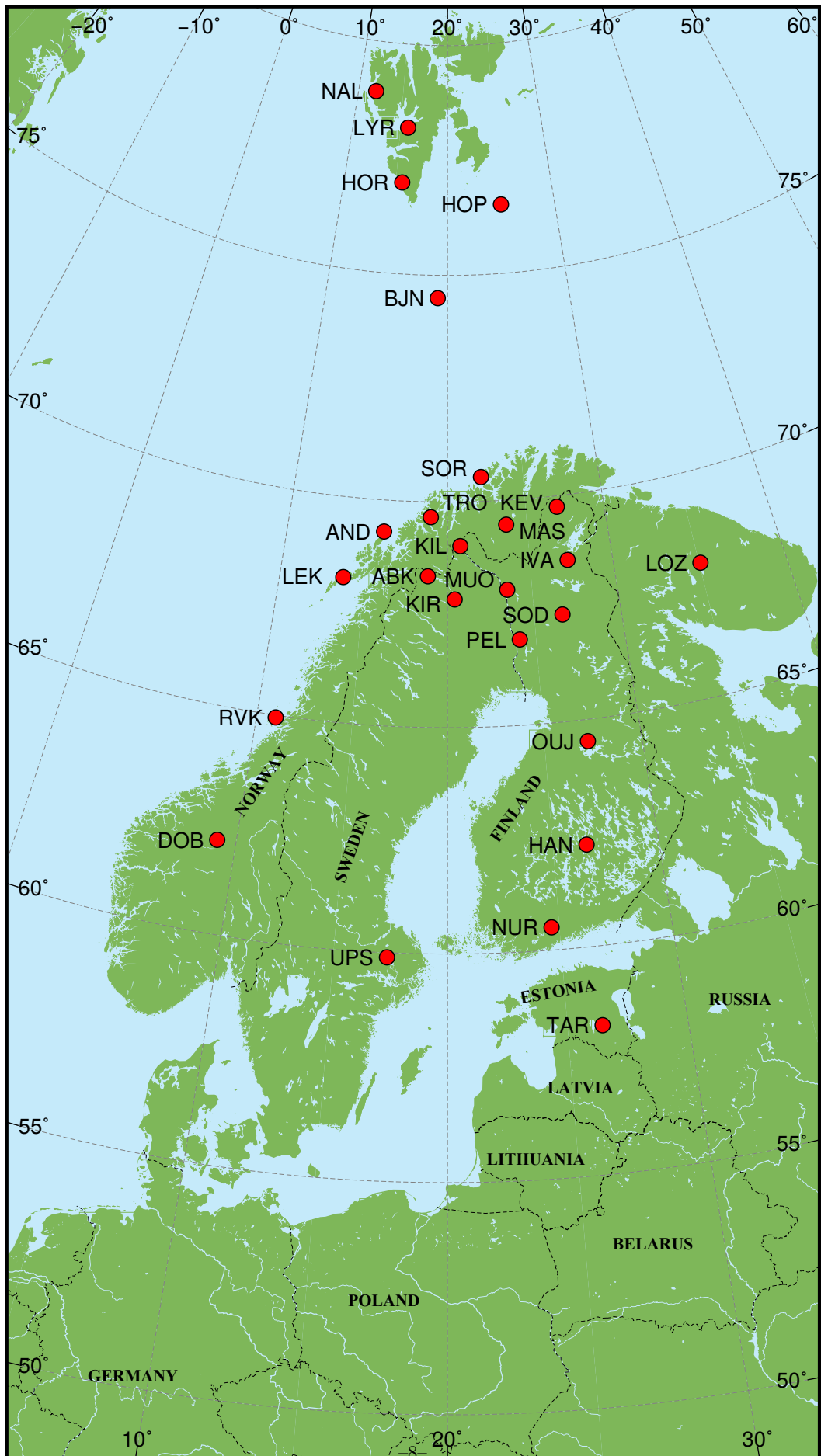


**Figure 1.** Location of IMAGE observatories with available data for 29 – 31 October 2003.

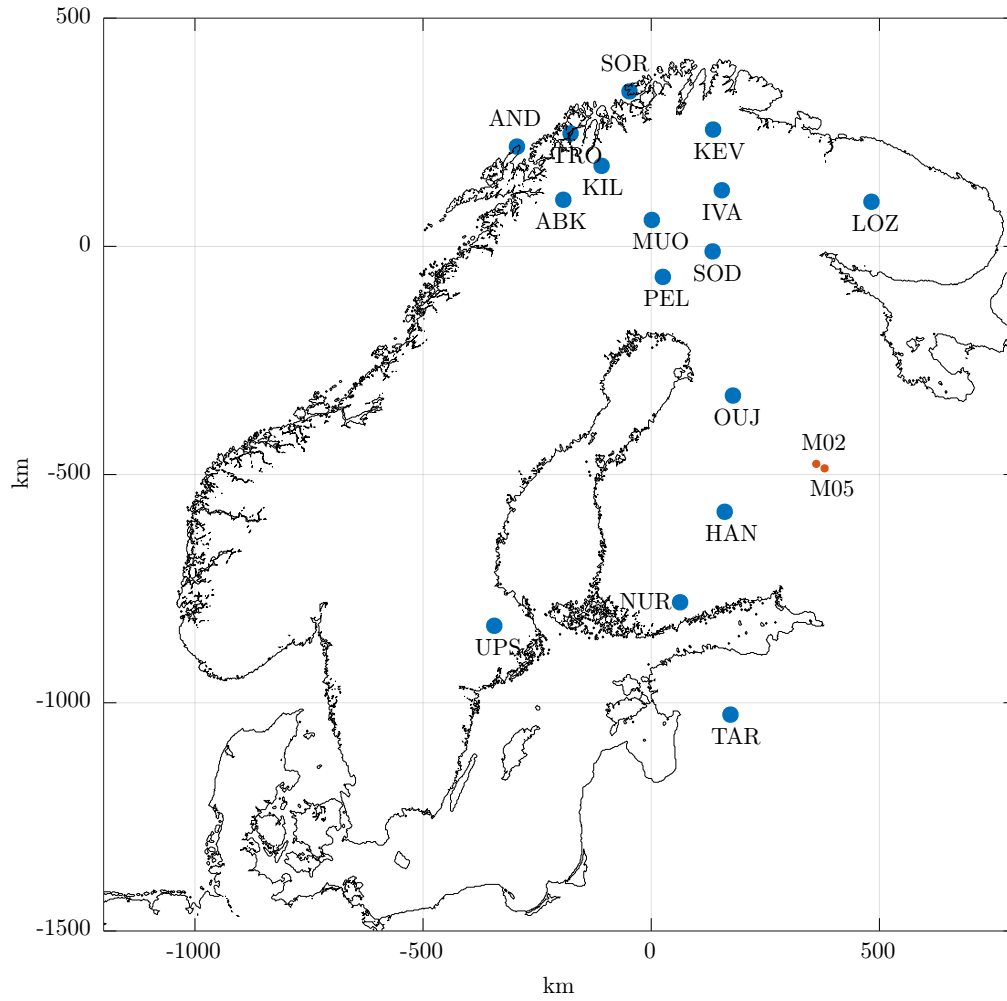


**Figure 2.** Location of IMAGE sites (blue-filled circles) used for GEF simulation (see Equation 6). Red circles – the location of sites where the GEF was measured and used for comparison with the simulated GEF.

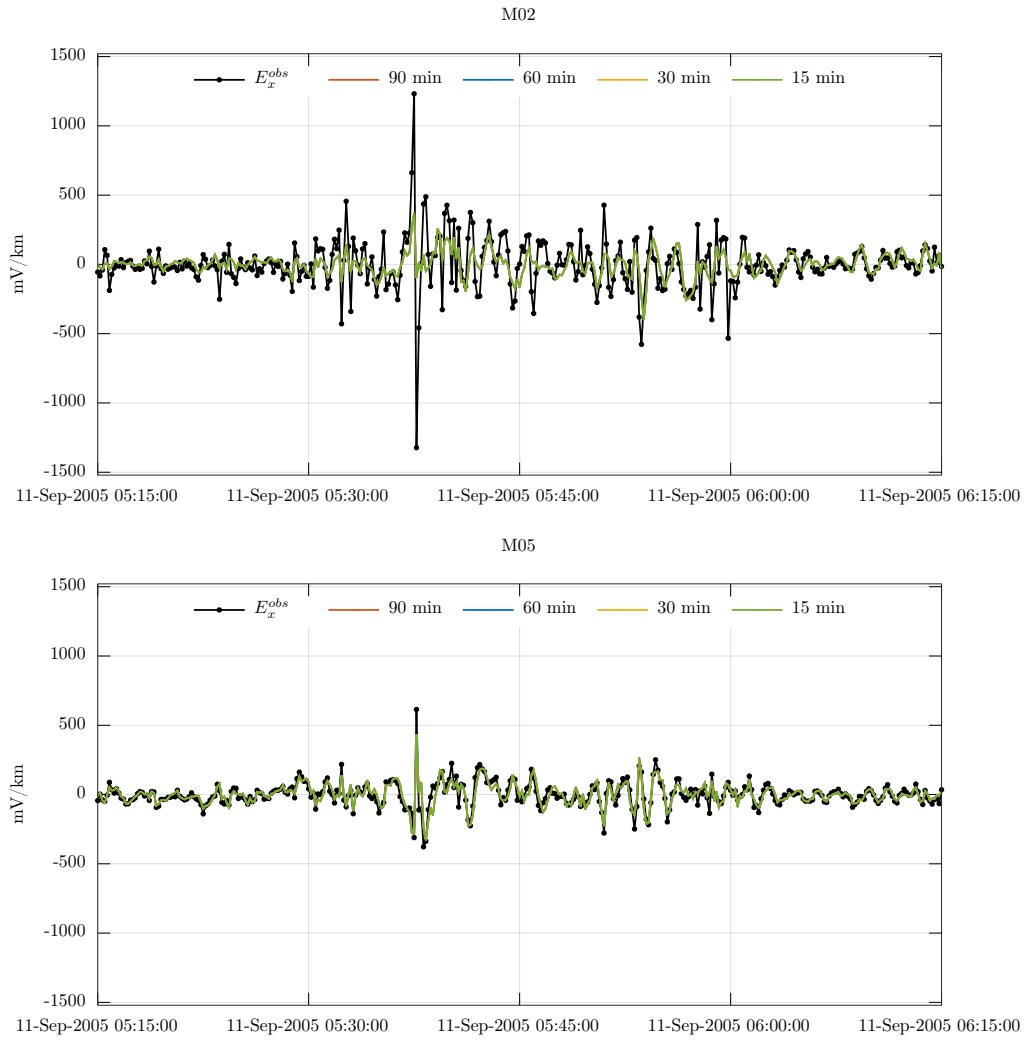


**Figure 3.** Comparison of the (geomagnetic) northward component of observed and modeled GEF at M02 and M05 sites for different values of  $T_{\Lambda}$ .

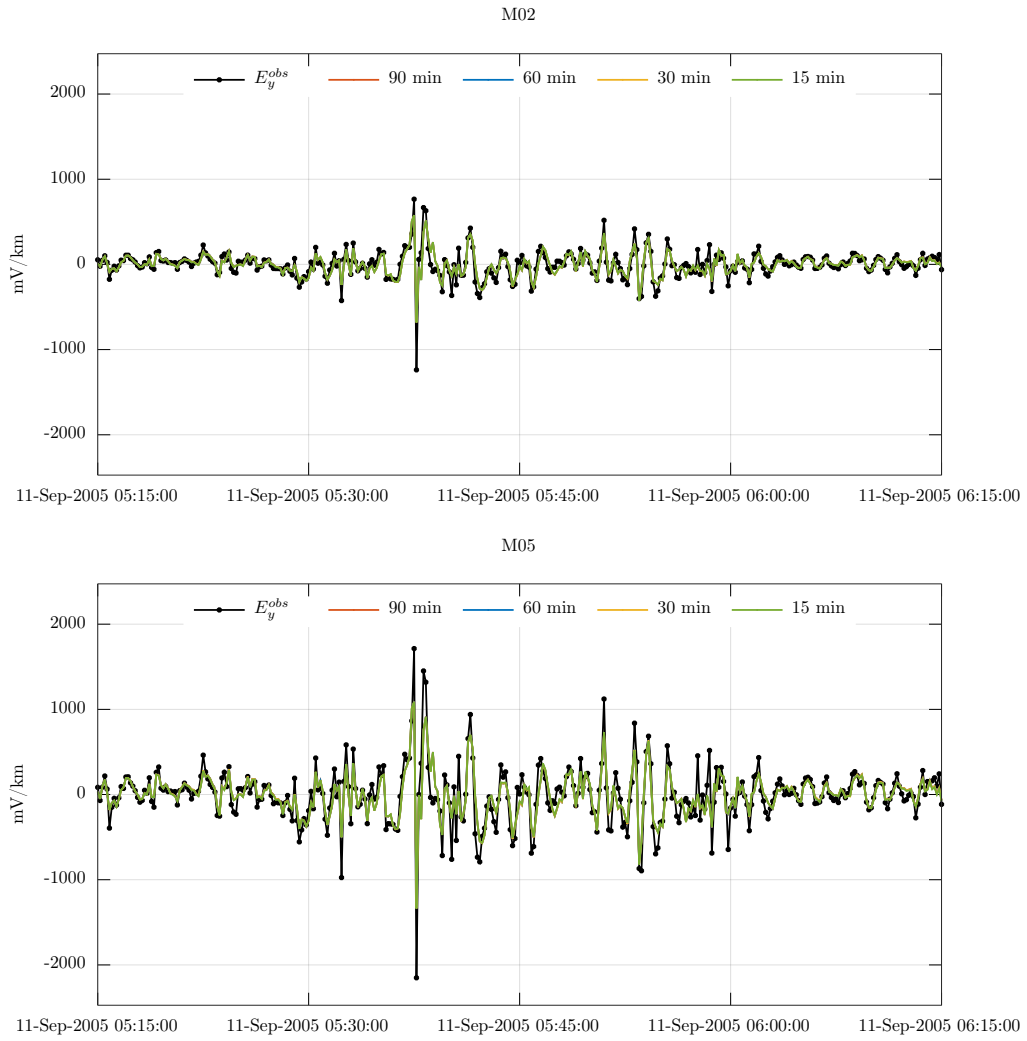


**Figure 4.** Comparison of the (geomagnetic) eastward component of observed and modeled GEF at M02 and M05 sites for different values of  $T_{\Lambda}$ .

**Table 1.** The agreement between modeled and observed GEF at site M02 in terms of correlation coefficients and coefficients of determination.

$T_\Lambda$ , min	Corr for $E_x$	Corr for $E_y$	$R^2$ for $E_x$	$R^2$ for $E_y$
15	0.635	0.881	0.371	0.768
30	0.633	0.881	0.370	0.767
60	0.632	0.881	0.369	0.767
90	0.632	0.880	0.369	0.766

**Table 2.** The agreement between modeled and observed GEF at site M05 in terms of correlation coefficients and coefficients of determination.

$T_\Lambda$ , min	Corr for $E_x$	Corr for $E_y$	$R^2$ for $E_x$	$R^2$ for $E_y$
15	0.882	0.891	0.777	0.767
30	0.882	0.890	0.778	0.766
60	0.882	0.890	0.778	0.766
90	0.882	0.890	0.778	0.766

244

#### 4 Comparing observed and modeled GIC

The conventional approach to simulate GIC in the pipelines is based on the following linear model (Boteler, 2013; Boteler & Pirjola, 2014)

$$GIC(\mathbf{r}, t) = \sum_{i=1}^M [a_i(\mathbf{r})E_x(\mathbf{r}_i, t) + b_i(\mathbf{r})E_y(\mathbf{r}_i, t)], \quad (12)$$

where  $M$  is the number of pipeline nodes and ends,  $\mathbf{r}_i$  – coordinates of their location, and  $\mathbf{r}$  is the coordinate of the pipeline point where GIC is recorded. Note that coefficients  $a_i$  and  $b_i$  are time-independent, but depend on pipeline physical parameters. In case when the conductivity distribution and the source are both laterally uniform, Equation (12) degenerates to

$$GIC(\mathbf{r}, t) = a(\mathbf{r})E_x(\mathbf{r}, t) + b(\mathbf{r})E_y(\mathbf{r}, t). \quad (13)$$

245

246

247

248

The formula (13) has been used in many studies (for example, Pulkkinen et al. (2001); Trichtchenko and Boteler (2002); Wawrzaszek et al. (2023)), but due to the obvious lateral nonuniformity of the conductivity distribution and the source in the region under investigation, we use Equation (12) to calculate GIC.

Having observed GIC and calculated GEF at many time instants, and bearing in mind that coefficients  $a_i$  and  $b_i$  are time-independent, we can form – as for elements of matrix  $D$  discussed in the previous section – highly over-determined SLE given by Equation (12) to estimate coefficients using the least-squares method. Precisely, these coefficients are calculated as the solution of the following SLE

$$a_1 E_x^{\text{mod}}(\mathbf{r}_1, t_i) + b_1 E_y^{\text{mod}}(\mathbf{r}_1, t_i) + \dots + a_M E_x^{\text{mod}}(\mathbf{r}_M, t_i) + b_M E_y^{\text{mod}}(\mathbf{r}_M, t_i) = GIC^{\text{obs}}(t_i), \quad (14)$$

249

250

251

252

253

where  $t_i$  runs multiple ( $K$ ) time instants. Here we omit the dependence of the coefficients and  $GIC^{\text{obs}}$  on  $\mathbf{r}$  because we have GIC's recordings only at one (Mäntsälä; MAN) point. Figure 5 shows the general geometry of the pipeline (gray lines) and location of 18 pipeline's nodes and ends (gold diamonds). The geometry of the pipeline is based on models presented in (Pulkkinen et al., 2001) and (Dimmock et al., 2019).

254

255

GIC measurements at the Mäntsälä point have been performed continuously since 1999; thus, we had an opportunity to compare observed and modeled GIC for a number of events.

**Table 3.** The agreement between modeled and observed GIC in terms of correlation coefficients and coefficients of determination for different events (substorms).

Substorms	Correlation	$R^2$
15 July – 16 July 2000	0.909	0.826
05 November – 06 November 2001	0.895	0.782
29 October – 1 November 2003	0.936	0.871

256 We have chosen events that happened in 2000, 2001, and 2003 years. It should be noted  
 257 that the approach we use to determine coefficients  $a_i$  and  $b_i$  is implicitly based an as-  
 258 sumption that the configuration of the pipeline system was the same during the events  
 259 in study. Concerning the relatively short period of 2000 – 2003, no major modifications  
 260 of the pipeline network were made. However, the present pipeline system is more exten-  
 261 sive than in the beginning of 2000's.

Note also that from 2005 the quality of GIC measurements degraded; this is why we considered earlier years' events. Also, note that the modeled GIC are calculated by reusing Equation (12)

$$GIC^{\text{mod}}(t) = \sum_{i=1}^M [a_i E_x^{\text{mod}}(\mathbf{r}_i, t) + b_i E_y^{\text{mod}}(\mathbf{r}_i, t)], \quad (15)$$

262 where  $a_i$  and  $b_i$  are obtained from the solution of the SLE (14). GEF in Equation (15)  
 263 were calculated using  $T_\Lambda = 15$  min; our model experiments (not shown in the paper) with  
 264 larger  $T_\Lambda$  reveal a negligible difference in the modeled GIC. As in the case of the GEF  
 265 comparison discussed in the previous section, we estimated  $a_i$  and  $b_i$  using GIC data not  
 266 from the time interval where we compare the results but using continuous data for 27 –  
 267 28 October 2003, giving  $K = 2 \times 24 \times 3600/10 = 17280$  equations to estimate respec-  
 268 tive  $2 \times M = 36$  coefficients.

269 Top two panels in Figures 6 – 8 demonstrate time series of observed and modeled  
 270 GIC for two 3-hour time intervals of corresponding years/months when large fluctuations  
 271 of GIC were detected. As one can see, the agreement between observed and modeled GIC  
 272 is remarkably good. The bottom right panels in the figures demonstrate the agreement  
 273 differently. It shows cross-plots of the observed and modeled GIC. Ideally, the observed  
 274 and modeled GIC would lie in a straight line, and this is indeed the case. Note that the  
 275 bottom left panel shows IMAGE observatories, the data from which were used to calcu-  
 276 late the GEF using Equation (6).

277 Finally, Table 3 demonstrates the agreement in a more quantitative way by pre-  
 278 senting correlation coefficients and coefficients of determination for the considered events.  
 279 One can see that both coefficients are close to 1, irrespective of the event. Interestingly,  
 280 the agreement in GIC is better than in GEF (see previous section). We attribute bet-  
 281 ter agreement in GIC to a smoothing effect of summation (see Equation (15)) which ef-  
 282 fectively suppresses the potential inaccuracy of modeled GEF at considered nodes and  
 283 ends.

## 284 5 Conclusions

285 This paper presents a novel approach to the GEF calculation in real time. The ap-  
 286 proach makes it possible to take into account the 3-D Earth's conductivity distribution  
 287 in the region and lateral variability of the source. It works with spatial modes describ-  
 288 ing the spatial structure of the source and exploits the multi-site (MS) transfer function

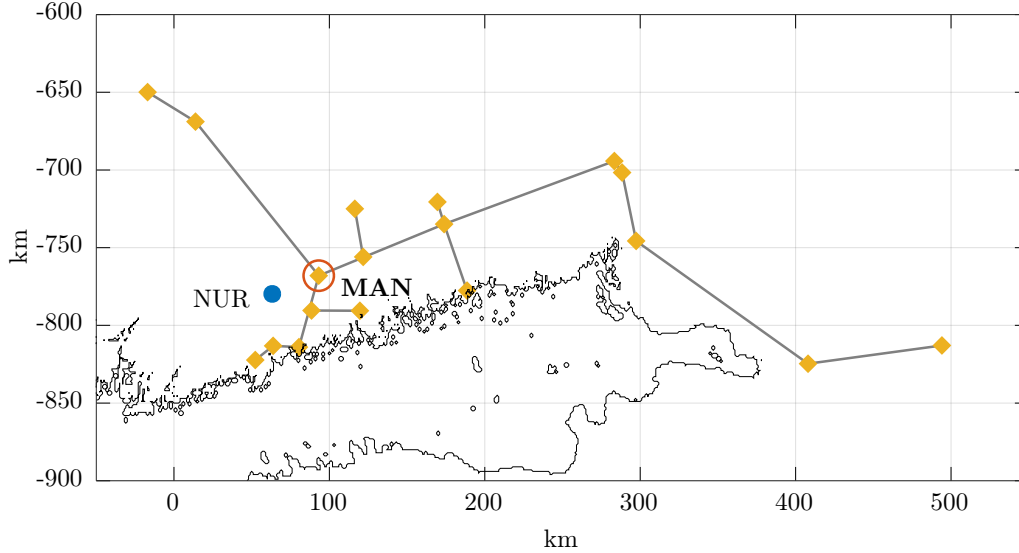


**Figure 5.** Geometry of the pipeline (grey lines) and location of 18 pipeline’s nodes and ends (gold diamonds); Mäntsälä (MAN) natural gas pipeline recording point (open red circle). For reference, the location of the IMAGE observatory, Nurmijärvi (NUR; blue-filled circle) is shown.

289 (TF) concept where MS TF relate the GEF at any location with horizontal magnetic  
 290 field at (fixed) multiple locations.

291 Using Fennoscandia as an example region and the SECS method to derive the spa-  
 292 tial modes, we compared the observed time series of the GEF and GIC available in the  
 293 region with those simulated using the proposed approach. Good agreement between ob-  
 294 served and modeled results validates the methodology. Notably, in contrast to the pre-  
 295 vious study (Marshalko et al., 2023), where GIC was calculated using the GEF at the  
 296 pipeline node where GIC is measured, in this paper, we considered a more realistic sce-  
 297 nario when GIC is calculated using simulated GEF at multiple nodes of the actual pipeline  
 298 grid.

299 While the simulations of GICs in this paper are mainly done for validation purposes,  
 300 the presented approach opens an avenue to derive a GIC activity indicator. Combining (6)  
 301 and (15) one can estimate GIC in real time. Moreover, as demonstrated in this paper,  
 302 the estimated GIC values correspond very accurately to the true recordings for a par-  
 303 ticular period when the conductor network can be assumed to be unchanged. Outside  
 304 of this period, the resulting GIC provides a meaningful proxy. Although it may not any  
 305 more give the true current, it can still be compared to other events in a relative sense.  
 306 For example, in our case, we could use the Halloween storm as a benchmark. Thus this  
 307 method has an immediate potential to be implemented as an operative product for space  
 308 weather services.

309 The prerequisite for the method’s application is continuous magnetic field measure-  
 310 ments at multiple locations, as in Fennoscandia. North America and China (with exist-  
 311 ing networks of magnetic field observations), or/and New Zealand (with the network of  
 312 variometers is being established now) are regions where the proposed method is worth  
 313 trying.

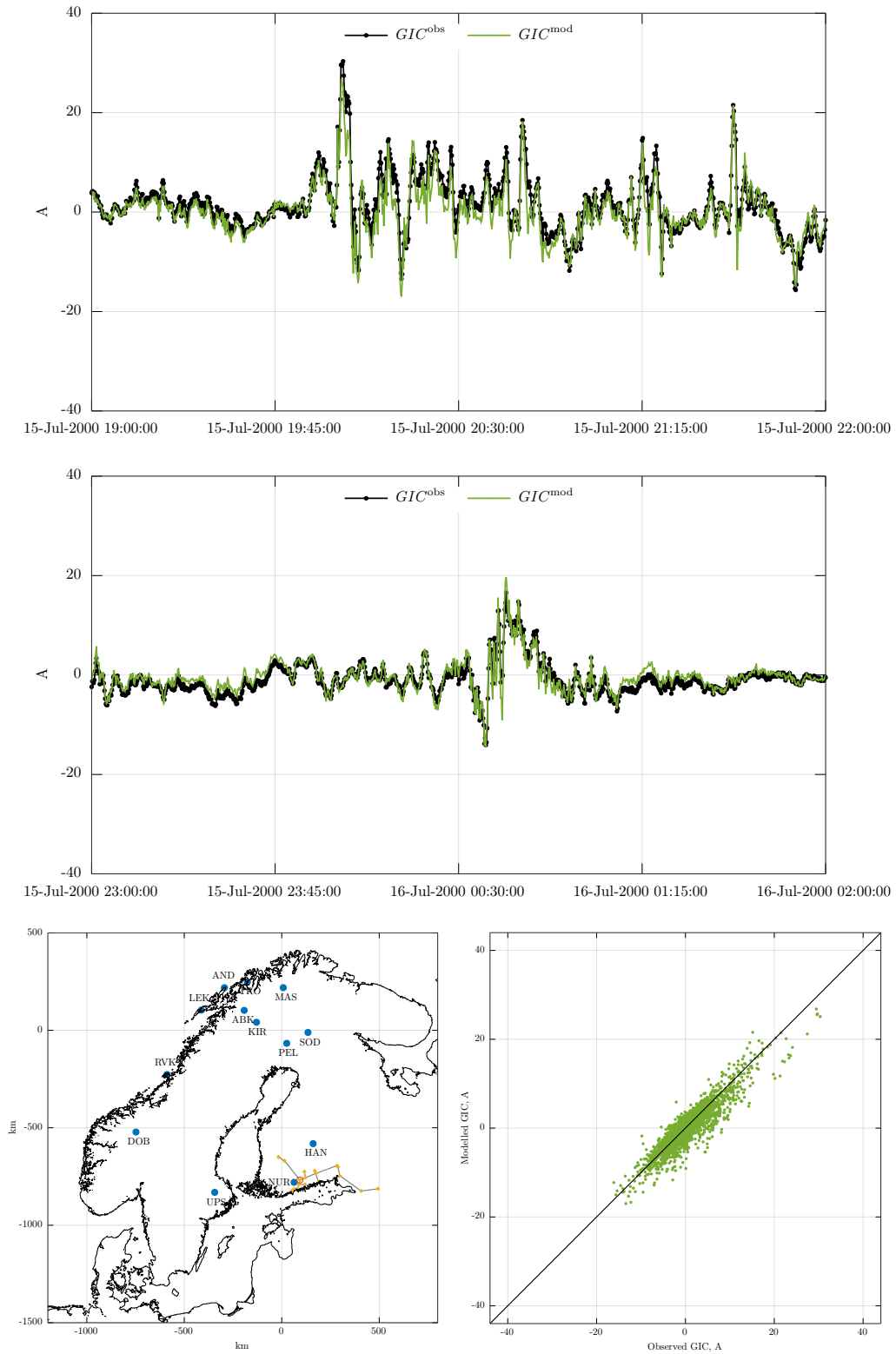


**Figure 6.** Substorms of 15/16 July 2000. Top two panels: comparison of observed and modeled GIC for two 3-hour time intervals. Bottom left panel: location of 13 IMAGE sites (blue-filled circles) used for the GEF simulation. Bottom right panel: cross-plots of observed and modeled GIC (cross-plots are demonstrated for the 2-day time interval: July 15 – 16 2000).

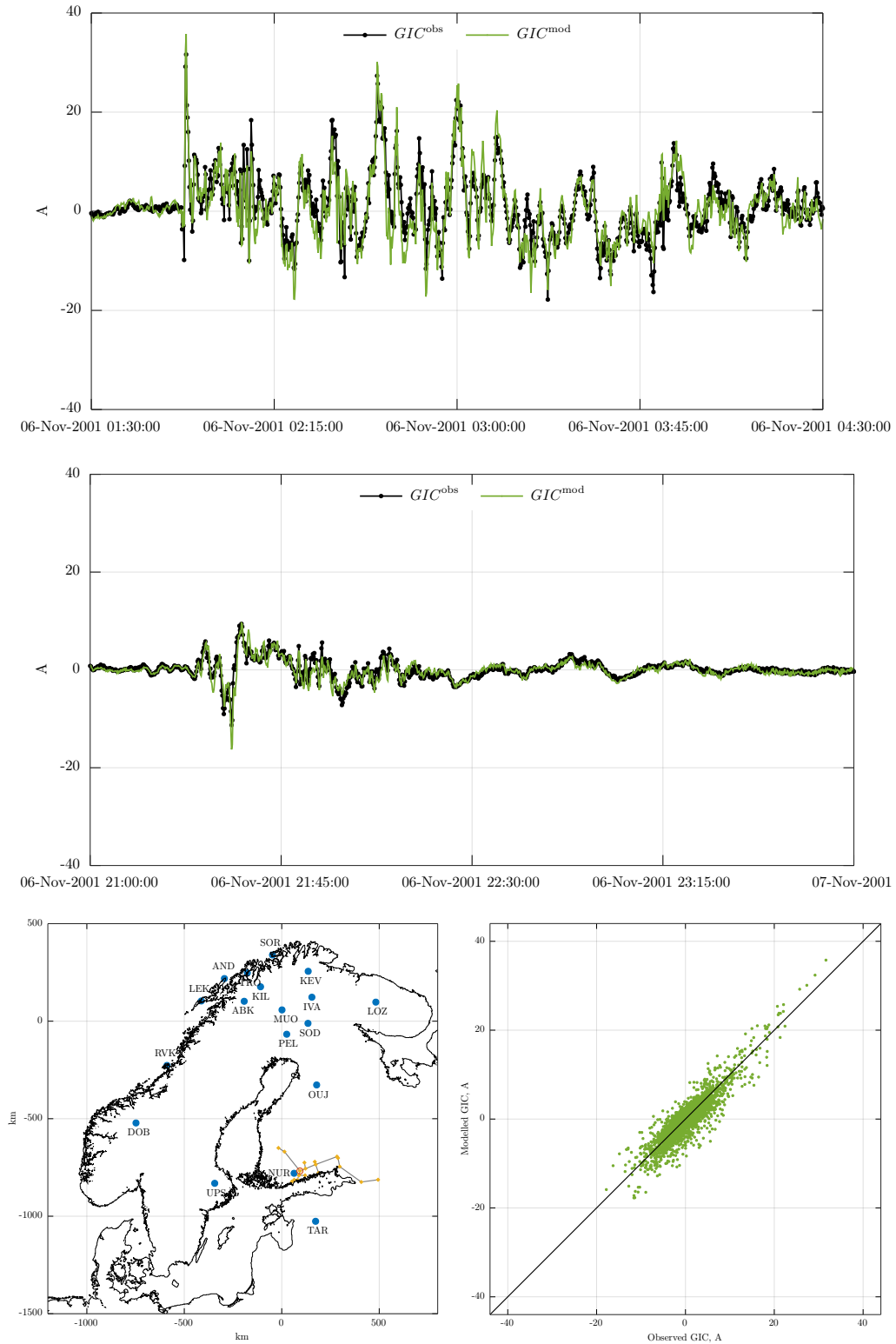


**Figure 7.** Substorms of 6 November 2001. Top two panels: comparison of observed and modeled GIC for two 3-hour time intervals. Bottom left panel: location of 18 IMAGE sites (blue-filled circles) used for the GEF simulation. Bottom right panel: cross-plots of observed and modeled GIC (cross-plots are demonstrated for the 2-day time interval: November 5 – 6 2001).

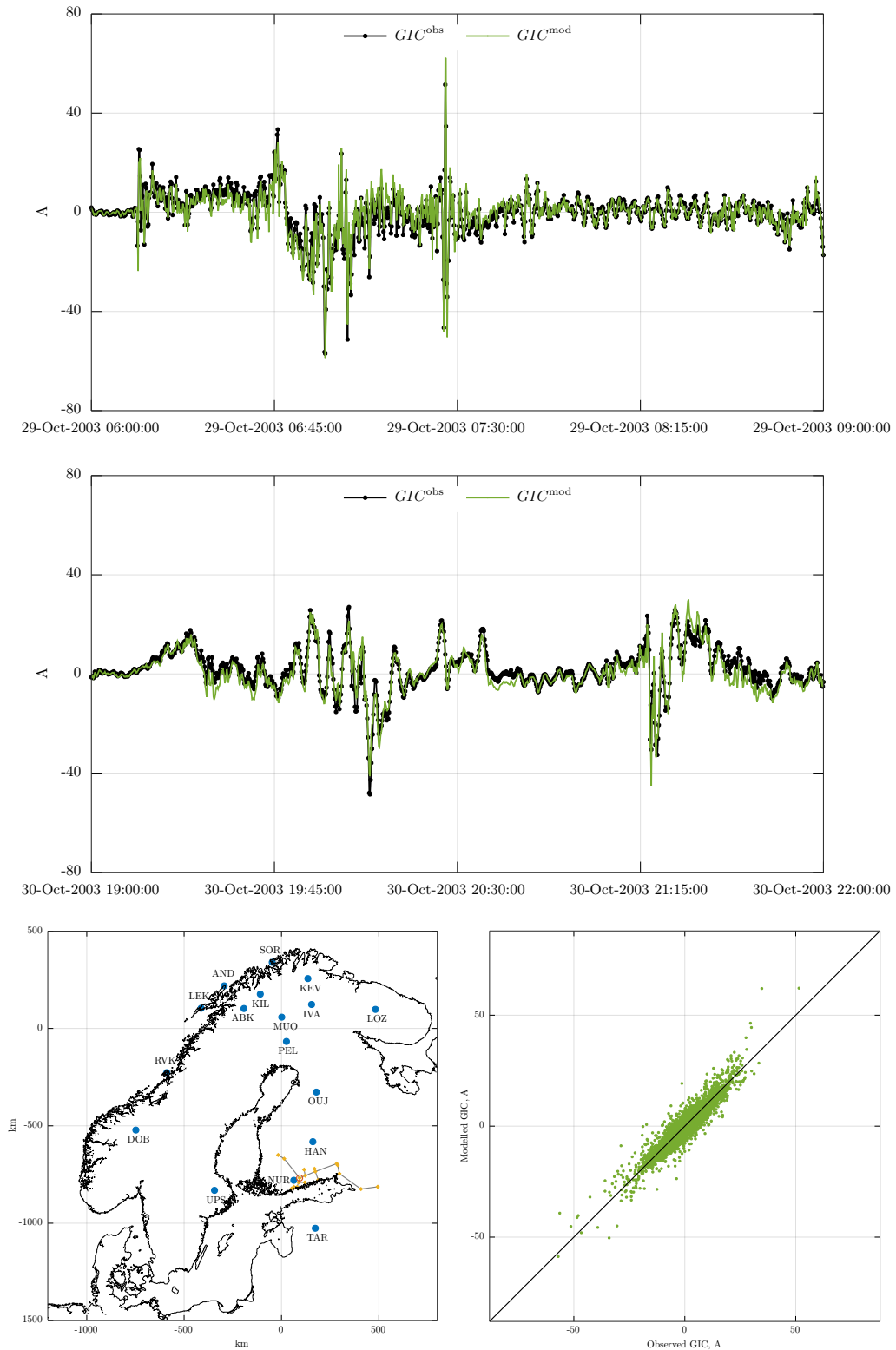


**Figure 8.** Substorms of 29/30 October 2003. Top two panels: comparison of observed and modeled GIC for two 3-hour time intervals. Bottom left panel: location of 17 IMAGE sites (blue-filled circles) used for the GEF simulation. Bottom right panel: cross-plots of observed and modeled GIC (cross-plots are demonstrated for the 3-day time interval: October 29 – November 1 2003).

314 It is worth noting that while comparing measured and simulated GEF at two se-  
 315 lected sites separated by only 21 km, we observe that experimental GEF at these sites  
 316 differ more significantly than the modeled GEF. Bearing in mind that the inducing source  
 317 (equivalent ionospheric current) is relatively (spatially) smooth, the most probable rea-  
 318 son for substantial lateral variability of the experimental GEF is local sharp lateral gra-  
 319 dients of the subsurface conductivity not accounted for in the used 3-D conductivity model  
 320 of the region. This prompts building a new – more accurate and detailed – 3-D conduc-  
 321 tivity model of Fennoscandia via a multi-scale 3-D inversion (using new modern inverse  
 322 solvers) of both old data (on which SMAP model was based) and a large amount of new  
 323 MT data collected in the region in the framework of various MT projects.

324 Finally, we have to mention that the proposed concept of multi-site transfer func-  
 325 tions can be easily adapted to another space weather related problem – accounting for  
 326 the geomagnetic disturbances during offshore directional drilling in northern seas (like  
 327 offshore of Alaska, Norway, British Isles, and North Russia), where magnetic field vari-  
 328 ations are routinely recorded at multiple adjacent land-based locations. In this scenario,  
 329 MS TF will relate magnetic field variations at sea bottom with those at multiple land-  
 330 based sites.

## 331 6 Open Research

332 The SMAP model (Korja et al., 2002) is available at the European Plate Observ-  
 333 ing System (EPOS) portal via EPOS (2019) (stored in JSON format and compressed  
 334 with bzip2) under CC BY-NC 4.0. PGIEM2G 3-D EM forward modeling code is avail-  
 335 able at Kruglyakov (2022) under GPLv2. GIC data are available at the website of the  
 336 Space and Earth Observation Centre of the Finnish Meteorological Institute (FMI) via  
 337 FMI (2023) under CC BY 4.0.

## 338 Acknowledgments

339 MK was supported by the New Zealand Ministry of Business, Innovation, & Employ-  
 340 ment through Endeavour Fund Research Programme contract UOOX2002. AK and MK  
 341 were also partially supported in the framework of Swarm DISC activities, funded by ESA  
 342 contract no. 4000109587, with support from EO Science for Society. EM and AV were  
 343 supported by grants 339329 from the Academy of Finland. We thank the institutes that  
 344 maintain the IMAGE Magnetometer Array: Tromsø Geophysical Observatory of UiT,  
 345 the Arctic University of Norway (Norway), Finnish Meteorological Institute (Finland),  
 346 Institute of Geophysics Polish Academy of Sciences (Poland), GFZ German Research Cen-  
 347 ter for Geosciences (Germany), Geological Survey of Sweden (Sweden), Swedish Insti-  
 348 tute of Space Physics (Sweden), Sodankylä Geophysical Observatory of the University  
 349 of Oulu (Finland), and Polar Geophysical Institute (Russia). We acknowledge Gasum  
 350 Oy for long-term collaboration in GIC studies of the Finnish natural gas pipeline.

## 351 References

- 352 Bailey, R., Halbedl, T. S., Schattauer, I., Achleitner, G., & Leonhardt, R. (2018).  
 353 Validating GIC models with measurements in Austria: Evaluation of accuracy  
 354 and sensitivity to input parameters. *Space Weather*, *16*(7), 887–902. doi:  
 355 10.1029/2018SW001842
- 356 Beggan, C. D. (2015). Sensitivity of geomagnetically induced currents to varying au-  
 357 roral electrojet and conductivity models. *Earth Planets Space*, *67*(24). doi: 10  
 358 .1186/s40623-014-0168-9
- 359 Beggan, C. D., Richardson, G. S., Baillie, O., Hübert, J., & Thomson, A. W. P.  
 360 (2021). Geoelectric field measurement, modelling and validation during  
 361 geomagnetic storms in the UK. *J. Space Weather Space Clim.*, *11*, 37.

- 362 <https://doi.org/10.1051/swsc/2021022> doi: 10.1051/swsc/2021022
- 363 Boteler, D. H. (2013, 01). A new versatile method for modelling geomagnetic induction  
364 in pipelines. *Geophysical Journal International*, *193*(1), 98-109. <https://doi.org/10.1093/gji/ggs113> doi: 10.1093/gji/ggs113
- 365 Boteler, D. H., & Pirjola, R. J. (2014). Comparison of methods for modelling  
366 geomagnetically induced currents. *Annales Geophysicae*, *32*(9), 1177–  
367 1187. <https://angeo.copernicus.org/articles/32/1177/2014/> doi:  
368 10.5194/angeo-32-1177-2014
- 369  
370 Campanyà, J., Gallagher, P. T., Blake, S. P., Gibbs, M., Jackson, D., Beggan,  
371 C. D., ... Hogg, C. (2019). Modeling geoelectric fields in Ireland and the  
372 UK for space weather applications. *Space Weather*, *17*(2), 216-237. <https://agupubs.onlinelibrary.wiley.com/doi/abs/10.1029/2018SW001999> doi:  
373 <https://doi.org/10.1029/2018SW001999>
- 374  
375 Dimmock, A. P., Rosenqvist, L., Hall, J.-O., Viljanen, A., Yordanova, E., Honko-  
376 nen, I., ... Sjöberg, E. C. (2019). The GIC and geomagnetic response over  
377 Fennoscandia to the 7-8 September 2017 geomagnetic storm. *Space Weather*,  
378 *17*(7), 989–1010. doi: 10.1029/2018SW002132
- 379 Divett, T., Ingham, M., Beggan, C. D., Richardson, G. S., Rodger, C. J., Thomson,  
380 A. W. P., & Dalzell, M. (2017). Modeling geoelectric fields and geomag-  
381 netically induced currents around New Zealand to explore GIC in the South  
382 Island's electrical transmission network. *Space Weather*, *15*(10), 1396–1412.  
383 doi: 10.1002/2017SW001697
- 384 Divett, T., Mac Manus, D. H., Richardson, G. S., Beggan, C. D., Rodger, C. J.,  
385 Ingham, M., ... Obana, Y. (2020). Geomagnetically induced current  
386 model validation from New Zealand's South Island. *Space Weather*, *18*(8),  
387 e2020SW002494. doi: 10.1029/2020SW002494
- 388 EPOS. (2019). *Dataset for "Crustal conductivity in Fennoscandia – a compilation of*  
389 *a database on crustal conductance in the Fennoscandian Shield"*, Korja et al.,  
390 2002, *Earth, Planets and Space* [Dataset]. European Plate Observing System  
391 (EPOS). [https://mt.research.ltu.se/MT/BEAR/1998/BEAR\\_3D.mod.json](https://mt.research.ltu.se/MT/BEAR/1998/BEAR_3D.mod.json)
- 392 FMI. (2023). *GIC recordings in the Finnish natural gas pipeline - ASCII files*  
393 [Dataset]. Finnish Meteorological Institute (FMI). [https://space.fmi.fi/gic/man\\_ascii/man.php](https://space.fmi.fi/gic/man_ascii/man.php)
- 394  
395 Honkonen, I., Kuvshinov, A., Rastätter, L., & Pulkkinen, A. (2018). Predicting  
396 global ground geoelectric field with coupled geospace and three-dimensional  
397 geomagnetic induction models. *Space Weather*, *16*(8), 1028–1041. doi:  
398 10.1029/2018SW001859
- 399 Jiracek, G. R. (1990). Near-surface and topographic distortions in electromagnetic  
400 induction. *Surv. Geophys.*, *11*, 163-203.
- 401 Kelbert, A., Balch, C., Pulkkinen, A., Egbert, G., Love, J., Rigler, J., & Fujii, I.  
402 (2017). Methodology for time-domain estimation of storm time geoelectric  
403 fields using the 3-D magnetotelluric response tensors. *Space Weather*, *15*(7),  
404 874–894. doi: doi:10.1002/2017SW001594
- 405 Korja, T., Engels, M., Zhamaletdinov, A. A., Kovtun, A. A., Palshin, N. A.,  
406 Smirnov, M. Y., ... BEAR Working Group (2002). Crustal conductivity  
407 in Fennoscandia – a compilation of a database on crustal conductance  
408 in the Fennoscandian Shield. *Earth, Planets and Space*, *54*, 535–558. doi:  
409 10.1186/BF03353044
- 410 Kruglyakov, M. (2022). *PGIEM2G* [Software]. Gitlab. [https://gitlab.com/m](https://gitlab.com/m.kruglyakov/PGIEM2G)  
411 [.kruglyakov/PGIEM2G](https://gitlab.com/m.kruglyakov/PGIEM2G)
- 412 Kruglyakov, M., & Kuvshinov, A. (2018). Using high-order polynomial basis in 3-D  
413 EM forward modeling based on volume integral equation method. *Geophysical*  
414 *Journal International*, *213*(2), 1387–1401. doi: 10.1093/gji/ggy059
- 415 Kruglyakov, M., Kuvshinov, A., & Marshalko, E. (2022). Real-time 3-D modeling of  
416 the ground electric field due to space weather events. A concept and its valida-

- 417 tion. *Space Weather*, 20(4), e2021SW002906. doi: 10.1029/2021SW002906
- 418 Kruglyakov, M., Kuvshinov, A., & Nair, M. (2022). A proper use of the adja-  
 419 cent land-based observatory magnetic field data to account for the geomag-  
 420 netic disturbances during offshore directional drilling. *Space Weather*. doi:  
 421 10.1029/2022SW003238
- 422 Kuvshinov, A., Grayver, A., Tøffner-Clausen, L., & Olsen, N. (2021). Probing 3-D  
 423 electrical conductivity of the mantle using 6 years of Swarm, CryoSat-2 and  
 424 observatory magnetic data and exploiting matrix Q-responses approach. *Earth,*  
 425 *Planets and Space*, 73, 67. doi: 10.1186/s40623-020-01341-9
- 426 Malone-Leigh, J., Companyà, J., Gallagher, P. T., Neukirch, M., Hogg, C., &  
 427 Hodson, J. (2023). Nowcasting geoelectric fields in Ireland using mag-  
 428 netotelluric transfer functions. *J. Space Weather Space Clim.*, 13, 6.  
 429 <https://doi.org/10.1051/swsc/2023004> doi: 10.1051/swsc/2023004
- 430 Marshalko, E., Kruglyakov, M., Kuvshinov, A., Juusola, L., Kwagala, N. K.,  
 431 Sokolova, E., & Pilipenko, V. (2021). Comparing three approaches to  
 432 the inducing source setting for the ground electromagnetic field modeling  
 433 due to space weather events. *Space Weather*, 19(2), e2020SW002657. doi:  
 434 10.1029/2020SW002657
- 435 Marshalko, E., Kruglyakov, M., Kuvshinov, A., Murphy, B. S., Rastätter, L.,  
 436 Ngwira, C., & Pulkkinen, A. (2020). Exploring the influence of lateral  
 437 conductivity contrasts on the storm time behavior of the ground electric  
 438 field in the eastern United States. *Space Weather*, 18(2), 159–195. doi:  
 439 10.1029/2019SW002216
- 440 Marshalko, E., Kruglyakov, M., Kuvshinov, A., & Viljanen, A. (2023). Rigorous  
 441 3-D modeling of the ground electric field in Fennoscandia during the Halloween  
 442 geomagnetic storm. *Space Weather, revision submitted. Preprint at ESS Open*  
 443 *Archive. DOI: 10.22541/essoar.167631318.88816433/v2.*
- 444 Marshall, R. A., Dalzell, M., Waters, C. L., Goldthorpe, P., & Smith, E. A. (2012).  
 445 Geomagnetically induced currents in the new zealand power network. *Space*  
 446 *Weather*, 10(8). [https://agupubs.onlinelibrary.wiley.com/doi/abs/](https://agupubs.onlinelibrary.wiley.com/doi/abs/10.1029/2012SW000806)  
 447 [10.1029/2012SW000806](https://doi.org/10.1029/2012SW000806) doi: <https://doi.org/10.1029/2012SW000806>
- 448 Marshall, R. A., Wang, L., Paskos, G. A., Olivares-Pulido, G., Van Der Walt, T.,  
 449 Ong, C., ... Yoshikawa, A. (2019). Modeling geomagnetically induced cur-  
 450 rents in Australian power networks using different conductivity models. *Space*  
 451 *Weather*, 17(5), 727–756. doi: <https://doi.org/10.1029/2018SW002047>
- 452 Nakamura, S., Ebihara, Y., Fujita, S., Goto, T., Yamada, N., Watari, S., &  
 453 Omura, Y. (2018). Time domain simulation of geomagnetically induced  
 454 current (GIC) flowing in 500-kv power grid in Japan including a three-  
 455 dimensional ground inhomogeneity. *Space Weather*, 16(12), 1946–1959. doi:  
 456 10.1029/2018SW002004
- 457 Pulkkinen, A., Lindahl, S., Viljanen, A., & Pirjola, R. (2005). Geomagnetic storm  
 458 of 29–31 October 2003: Geomagnetically induced currents and their relation  
 459 to problems in the Swedish high-voltage power transmission system. *Space*  
 460 *Weather*, 3(8), S08C03. doi: 10.1029/2004SW000123
- 461 Pulkkinen, A., Viljanen, A., Pajunpää, K., & Pirjola, R. (2001). Recordings  
 462 and occurrence of geomagnetically induced currents in the Finnish natural  
 463 gas pipeline network. *Journal of Applied Geophysics*, 48(4), 219–231. doi:  
 464 10.1016/S0926-9851(01)00108-2
- 465 Püthe, C., Manoj, C., & Kuvshinov, A. (2014). Reproducing electric field ob-  
 466 servations during magnetic storms by means of rigorous 3-D modelling and  
 467 distortion matrix co-estimation. *Earth, Planets and Space*, 66, 162–171.
- 468 Rodger, C. J., Mac Manus, D. H., Dalzell, M., Thomson, A. W. P., Clarke, E.,  
 469 Petersen, T., ... Divett, T. (2017). Long-term geomagnetically induced  
 470 current observations from new zealand: Peak current estimates for ex-  
 471 treme geomagnetic storms. *Space Weather*, 15(11), 1447–1460. <https://>

- 472 [agupubs.onlinelibrary.wiley.com/doi/abs/10.1002/2017SW001691](https://doi.org/10.1002/2017SW001691) doi:  
473 <https://doi.org/10.1002/2017SW001691>
- 474 Rosenqvist, L., & Hall, J. O. (2019). Regional 3-D modeling and verification of ge-  
475 omagnetically induced currents in Sweden. *Space Weather*, *17*(1), 27–36. doi:  
476 10.1029/2018SW002084
- 477 Smirnov, M., Korja, T., & Pedersen, L. (2006). Electromagnetic Mini Array  
478 (EMMA) Project in Fennoscandia Looking into Deep Lithosphere. In *Pro-*  
479 *ceedings of the 7th International Conference: PROBLEMS OF GEOCOSMOS,*  
480 *St. Petersburg.*
- 481 Tanskanen, E. I. (2009). A comprehensive high-throughput analysis of substorms ob-  
482 served by IMAGE magnetometer network: Years 1993–2003 examined. *J. Geo-*  
483 *phys. Res.*, *114*(A5). doi: 10.1029/2008JA013682
- 484 Trichtchenko, L., & Boteler, D. H. (2002). Modelling of geomagnetic induc-  
485 tion in pipelines. *Annales Geophysicae*, *20*(7), 1063–1072. [https://](https://angeo.copernicus.org/articles/20/1063/2002/)  
486 [angeo.copernicus.org/articles/20/1063/2002/](https://angeo.copernicus.org/articles/20/1063/2002/) doi: 10.5194/angeo-20  
487 -1063-2002
- 488 Vanhamäki, H., & Juusola, L. (2020). Introduction to Spherical Elementary Current  
489 Systems. In M. W. Dunlop & H. Lühr (Eds.), *Ionospheric multi-spacecraft*  
490 *analysis tools: Approaches for deriving ionospheric parameters* (pp. 5–33).  
491 Cham: Springer International Publishing. doi: 10.1007/978-3-030-26732-2\_2
- 492 Viljanen, A., & Pirjola, R. (1994). Geomagnetically induced currents in the Finnish  
493 high-voltage power system. A geophysical review. *Surv. Geophys.*, *15*, 383–408.  
494 doi: 10.1007/BF00665999
- 495 Viljanen, A., Pirjola, R., Wik, M., Ádám, A., Prácsér, E., Sakharov, Y., & Katkalov,  
496 J. (2012). Continental scale modelling of geomagnetically induced currents. *J.*  
497 *Space Weather Space Clim.*, *2*, A17. doi: 10.1051/swsc/2012017
- 498 Viljanen, A., Pulkkinen, A., Pirjola, R., Pajunpää, K., Posio, P., & Koistinen, A.  
499 (2006). Recordings of geomagnetically induced currents and a nowcasting ser-  
500 vice of the Finnish natural gas pipeline system. *Space Weather*, *4*(10). doi:  
501 10.1029/2006SW000234
- 502 Wang, L., Lewis, A. M., Ogawa, Y., Jones, W. V., & Costelloe, M. T. (2016). Mod-  
503 eling geomagnetic induction hazards using a 3-D electrical conductivity model  
504 of Australia. *Space Weather*, *14*, 1125–1135. doi: 10.1002/2016SW001436
- 505 Wawrzaszek, A., Gil, A., Modzelewska, R., Tsurutani, B. T., & Wawrzaszek, R.  
506 (2023). Analysis of large geomagnetically induced currents during the 7–8  
507 september 2017 storm: Geoelectric field mapping. *Space Weather*, *21*(3),  
508 e2022SW003383. doi: <https://doi.org/10.1029/2022SW003383>